Frequency-wavenumber spectrum of the free surface of shallow turbulent flows over a rough boundary

G. Dolcetti, K. V. Horoshenkov, A. Krynkin, and S. J. Tait

Articles you may be interested in

Laminar and turbulent flows over hydrophobic surfaces with shear-dependent slip length
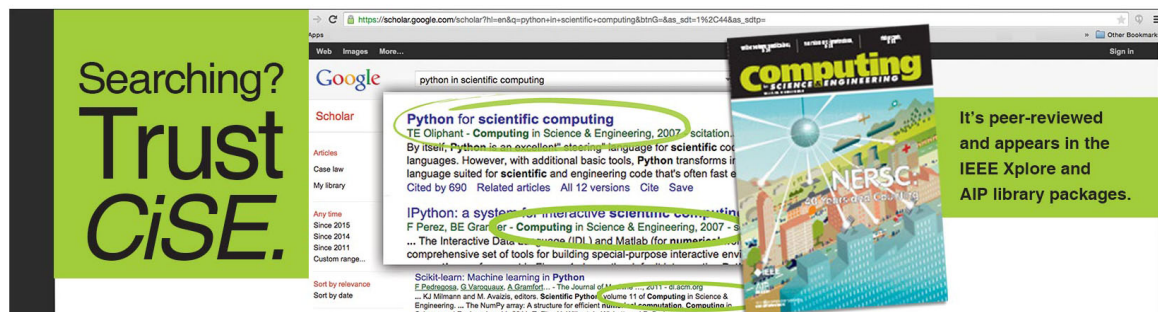Phys. Fluids **28**, 035109 (2016); 10.1063/1.4943671

Surface deformations and wave generation by wind blowing over a viscous liquid
Phys. Fluids **27**, 122103 (2015); 10.1063/1.4936395

Direct numerical simulation of turbulent flow in a rotating square duct
Phys. Fluids **27**, 065104 (2015); 10.1063/1.4922087

Understanding turbulent flow over ripple-shaped random roughness in a channel
Phys. Fluids **24**, 115102 (2012); 10.1063/1.4761836

Asymmetries in an obstructed turbulent channel flow
Phys. Fluids **22**, 095103 (2010); 10.1063/1.3478974

Frequency-wavenumber spectrum of the free surface of shallow turbulent flows over a rough boundary

G. Dolcetti,[1,a] K. V. Horoshenkov,[1] A. Krynkin,[1] and S. J. Tait[2]

[1]*Department of Mechanical Engineering, The University of Sheffield, Sheffield S1 3JD, United Kingdom*
[2]*Department of Civil and Structural Engineering, The University of Sheffield, Sheffield S1 3JD, United Kingdom*

Data on the frequency-wavenumber spectra and dispersion relation of the dynamic water surface in an open channel flow are very scarce. In this work, new data on the frequency-wavenumber spectra were obtained in a rectangular laboratory flume with a rough bottom boundary, over a range of subcritical Froude numbers. These data were used to study the dispersion relation of the surface waves in such shallow turbulent water flows. The results show a complex pattern of surface waves, with a range of scales and velocities. When the mean surface velocity is faster than the minimum phase velocity of gravity-capillary waves, the wave pattern is dominated by stationary waves that interact with the static rough bed. There is a coherent three-dimensional pattern of radially propagating waves with the wavelength approximately equal to the wavelength of the stationary waves. Alongside these waves, there are freely propagating gravity-capillary waves that propagate mainly parallel to the mean flow, both upstream and downstream. In the flow conditions where the mean surface velocity is slower than the minimum phase velocity of gravity-capillary waves, patterns of non-dispersive waves are observed. It is suggested that these waves are forced by turbulence. The results demonstrate that the free surface carries information about the underlying turbulent flow. The knowledge obtained in this study paves the way for the development of novel airborne methods of non-invasive flow monitoring. © *2016 Author(s). All article content, except where otherwise noted, is licensed under a Creative Commons Attribution (CC BY) license (http://creativecommons.org/licenses/by/4.0/).* [http://dx.doi.org/10.1063/1.4964926]

I. INTRODUCTION

The study of the free surface of the sea has received considerable attention in the past. Since the fundamental work of Miles[1] and Phillips,[2] the various mechanisms that allow the wind to produce characteristic patterns of gravity-capillary waves have been well known. The understanding of these phenomena facilitated greatly the development of remote monitoring techniques, which thereafter became a formidable aid to the study of ocean dynamics.[3] In comparison with the surface of the ocean, the free surface of shallow flows such as rivers and in manmade open channels is less understood. Understanding of the relationship between the rough static bed and the turbulence processes in the shallow flow and the resultant free surface pattern is important for the development of acoustic, radar, and optical monitoring techniques, which may enable us to measure the hydraulic processes remotely.[4]

The mechanism that is mostly responsible for the generation of the wave patterns at the free surface of a shallow water turbulent flow has not been unambiguously identified yet. A number of researchers have focused on the boils and scars that form at the free surface due to the direct interaction with turbulent coherent structures such as large scale vortices (for a classification of these

---

a)Author to whom correspondence should be addressed. Electronic mail: gdolcetti1@sheffield.ac.uk

28, 105105-1

phenomena see the work of Nezu and Nakagawa[5] and Brocchini and Peregrine[6]). These patterns have been studied both experimentally[7,8] and numerically.[9,10] In shallow open channel turbulent flows the effect of gravity is dominating, but the turbulence can effectively disturb the free surface to the point of breaking.[6] The correlation between the free surface elevation and the flow vorticity or turbulent velocities is high in numerical simulations,[10] but generally much lower in experiments,[11,12] where it is difficult to obtain high quality data near the surface, and dispersive waves can affect the correlation locally.[11]

The bed topography can also generate patterns of gravity-capillary waves. The amplitude of these patterns depends on the two-dimensional spatial spectrum of the bed roughness, and they propagate in space and in time.[13] When the flow velocity exceeds the minimum phase velocity of gravity-capillary waves, stationary patterns of waves can develop. If the wave amplitude is small, these patterns can be determined from the linearized free surface equations derived for an irrotational flow.[14] Additional unsteady patterns such as periodic successions of solitons or cnoidal waves propagating upstream require a nonlinear analysis.[15]

The vertical variation of the streamwise velocity in a shallow flow complicates the analytical treatment of the problem. The dispersion relation changes when the vertical velocity profile is considered, and so does the wavenumber of the stationary waves.[16,17] The flow rotationality can also promote the growth of resonant waves. The resonant growth of freely propagating gravity waves in a sheared flow has been studied both as the result of the (laminar) critical layer instability[18,19] and of the interaction with turbulent pressure fluctuations.[20] Teixeira and Belcher[20] also described the growth of non-resonant forced waves, which do not satisfy the dispersion relation of gravity-capillary waves but have the same velocity of the pressure turbulence perturbation.

There has been a very limited number of numerical[21,22] or experimental[11] studies that tried to quantify the frequency-wavenumber spectrum of the waves on a free surface turbulent flow. The numerical simulations[21,22] show patterns of forced waves similar to the ones predicted by the model of Teixeira and Belcher,[20] in which the frequency is governed by the turbulent forcing, as well as shorter freely propagating patterns following the dispersion relation of gravity-capillary waves. The measurements reported by Savelsberg and van de Water[11] are the only known experimental results that describe the dispersion of the surface patterns on shallow turbulent flows in three-dimensions, but they are focused on grid-generated turbulence which is not representative of the turbulence in open channel shallow flows. The spectral resolution of their spectra was limited. This hindered the observation of the dispersion relation near the dominant scales and did not allow for definitive conclusions on the generation mechanism of the observed free surface patterns.

This paper aims to address the apparent lack of experimental data on the spectrum and dispersion relations of the waves generated on the surface of a turbulent free surface flow. The purpose of this work is to test the following four hypotheses: (i) that the interaction with the rough bed produces patterns of gravity waves on the free surface, and that their dispersion relationship can be predicted by taking into account the vertical profile of the streamwise velocity. (ii) That large coherent turbulent structures in the flow also produce patterns on the free surface, which advect at the velocity close to the velocity of the flow near the surface. (iii) That the first of these two mechanisms is the dominant one when the mean surface velocity is larger than the minimum phase velocity of the gravity-capillary waves, and that it produces stationary waves which govern the typical temporal and spatial scales of the free surface of a shallow turbulent flow. (iv) That the free surface of a turbulent shallow flow becomes progressively more rough as the characteristic Froude number increases.

In order to test these hypotheses, a set of 13 experiments was performed in a rectangular laboratory flume with rough bed for a wide range of flow conditions. Two orthogonal arrays of wave probes were used to measure the frequency-wavenumber spectrum of the free surface fluctuations in the streamwise and transverse directions. This allowed the quasi-3D characterization of the dynamic behaviour of the free surface.

This paper is organized as follows. Section II describes the experimental setup. Section III summarizes the analysis procedure that allowed the determination of the frequency-wavenumber spectrum of the free surface. This includes an iterative algorithm for the reconstruction of the spatial correlation function on a uniform set of spatial locations, which is described in the Appendix. Section IV presents the derivation of the free surface dispersion relation in an inviscid incompressible

flow with a power function velocity profile, which was used to interpret the experimental data. Section V presents the experimental results, which are discussed in Section VI. The final conclusions are drawn in Section VII.

II. EXPERIMENTAL SETUP

A. Experimental flume

All the experiments were performed in a rectangular laboratory flume with a fixed roughened bed. The flume was 12.6 m long and 0.459 m wide. An adjustable gate at the downstream end of the flume ensured that the mean flow depth was uniform along the channel. The flow discharge and the flume bed slope were controlled in order to obtain the desired flow mean depth and velocity. The channel bed was covered with three layers of hexagonally packed plastic spheres with the diameter $d = 25.4$ mm. The uniform flow depth H was measured by a set of manual point gauges distributed along the channel at various locations in the longitudinal and transverse directions. The accuracy of the depth measurements is estimated to be ±0.5 mm. The depth datum should be defined such that the streamwise velocity distribution is best fitted by the Nikuradse logarithmic law, of which the power function profile is an approximation. In the case of a bed of spheres, the datum is in the range of $0.15d$ to $0.3d$ below the crests of the spheres.[5] Here the datum was set at the distance $d/4$ below the crests in accordance with the results of Nakagawa, Nezu, and Ueda.[23]

The mean streamwise surface velocity U_0 was measured by timing the passage of neutrally buoyant floats along a streamwise distance of 1.53 m and taken as the average of 10 successive measurements. The maximum standard deviation across the 10 velocity measurements was found to be smaller than 3.5% of U_0. The characteristic Froude number, $F = U_0/\sqrt{gH}$, was determined from the mean surface velocity and the uniform mean flow depth.[17] The depth-averaged velocity, U_H, was calculated from the flow discharge and from the flow area determined by the uniform flow depth and the channel width. The discharge was measured using a U tube manometer and a calibrated orifice plate in the inlet pipe.

Measurements of the average streamwise velocity profiles were performed previously using a particle image velocimetry system over the same rough bed and are detailed by Nichols.[4] The analysis of these data indicate that the power function profile

$$U = U_0(z/H)^n \tag{1}$$

approximates the shape of the measured velocity distributions within ±8% of the local mean velocity $U(z)$ in the range $0.2 < z/H < 0.8$. The values of n which provided the best interpolation to the data reported by Nichols[4] are shown in Fig. 1. These were compared to the predictions by Cheng[24] (equations 34 and 35, p. 1781, with the relation $n^{-1}\sqrt{f} = 1.0$, where f is the friction factor) at $Re_H = 10^4$ and $Re_H = 5 \times 10^5$. The Reynolds number Re_H was based on the depth-averaged velocity U_H and defined as $Re_H = 4\rho U_H H \mu^{-1}$, in accordance with Cheng.[24] In the measurements of Nichols, Re_H varied between 4.7×10^4 and 2.9×10^5, while n varied from $1/2.4$ at the submergence $H/d = 1.7$ to $1/3.3$ at the submergence $H/d = 4$, with a minimum $n = 1/3.8$ at $H/d = 3.6$. In
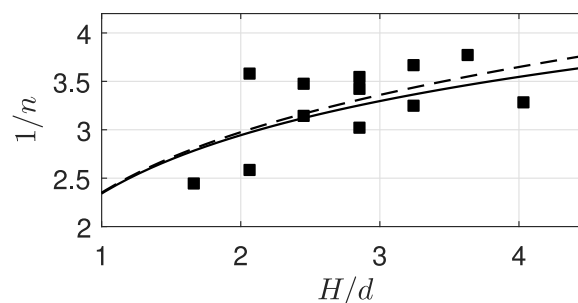

FIG. 1. The exponent n of the power-function average streamwise velocity profile in the flume: (squares) best interpolation to the velocity profile data measured by Nichols,[4] (lines) prediction[24] assuming $n^{-1}\sqrt{f} = 1.0$ for (dashed) $Re_H = 10^4$, and (solid) $Re_H = 5 \times 10^5$.

the measurements reported here, $3.0 \times 10^4 \le Re_H \le 2.1 \times 10^5$ and $1.6 \le H/d \le 4.0$. The expected values of n based on the formula proposed by Cheng[24] were between 1/2.8 and 1/3.5. These values are reported for each condition in Table II. $n = 1/3$ was selected as a representative value. In the range of flow conditions and frequencies described here, the maximum difference between the dispersion relation (Equations (7) and (12)) with $n = 1/2.8$ and $n = 1/3.6$ was equal to 2.3 rad/m, measured along the wavenumber axis. The maximum difference when n varied from $n = 1/2.4$ to $n = 1/3.8$ was equal to 4.5 rad/m. These differences were comparable to the maximum resolution of the measurements in this study, which was estimated as 4.05 rad/m.

B. Surface elevation measurements with non-equidistant arrays of waveprobes

Wave probes provide an attractive alternative to several optical methods which are harder to implement on a flow in a flume with a rough non-transparent bed, although the optical methods generally have a better spatial resolution. The surface gradient detector developed by Zhang and Cox[25] was applied successfully by Dabiri and Gharib[26] and Dabiri[27] to the study of the free surface of a horizontally sheared flow. However, the size of the measurement area in these studies was very limited. The free surface synthetic Schlieren method described by Moisy, Rabaud, and Salsac[28] is based on the refraction of non-collimated light at the free surface and uses a random pattern of dots. Savelsberg and van de Water[11] measured the frequency-wavenumber spectrum of the free surface slope in two orthogonal directions also from the refraction of a scanning laser beam. Refraction-based methods require either the light source to be immersed in water or the flow bottom to be transparent; therefore, they are not practical for a flume with a rough non-transparent boundary. The Fourier transform profilometry technique[29] was extended to the measurement of the water free surface by Cobelli *et al.*[30] and Maurel *et al.*[31] and is based on the airborne projection of a two-dimensional fringe pattern on the free surface. This method was applied to the measurement of the frequency-wavenumber spectrum of gravity-capillary wave turbulence in a wave tank by Herbert, Mordant, and Falcon,[32] Cobelli *et al.*,[33] and Aubourg and Mordant.[34] The technique requires adding a white dye to the water in order to improve its light diffusivity. This requirement makes the profilometry technique less practical for this study due to the large amount of water recirculated by the laboratory system, the large test area size, and the practical issues with the disposal of dyed water. For these reasons, a setup with arrays of waveprobes was adopted in the experiments. It provided the temporal and spatial resolution desired in this study.

The instantaneous surface elevation was measured in time by 16 conductance wave probes arranged non-equidistantly in two orthogonal arrays. Each probe comprised of two 0.24 mm thick vertical tinned copper wires that were anchored separately to the flume bed. The two wires were tensioned and parallel and aligned along the transverse y-direction. An alternating current was passed through the wires, so that the voltage at their free ends was a function of the water conductivity and varied linearly with the instantaneous surface elevation. Two arrays of wave probes were employed, one in the streamwise x-direction (8 probes, $1_{(x)}$, $2_{(x)}$, ..., $8_{(x)}$) along the flume centreline and the other in the transverse y-direction (8 probes, $1_{(y)}$, $2_{(y)}$, ..., $8_{(y)}$). The spatial arrangement of these two arrays is shown in Fig. 2. The coordinates of the probes for all arrays are
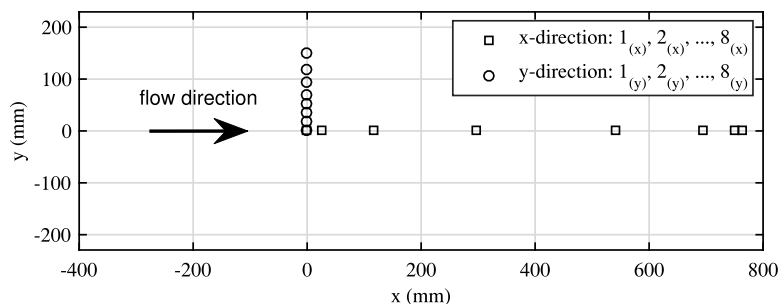
FIG. 2. The arrangement of the wave probe arrays. The origin of the x-y coordinates is 9 m downstream from the flume inlet, along the centreline.

TABLE I. The spatial distribution of the conductance wave probes for the two arrays.

Array	Probe location[a] (mm)							
	1	2	3	4	5	6	7	8
x-direction	0	26.0	116.5	297.5	541.5	694.5	750.0	762.5
y-direction	0	17.5	35.0	51.5	69.0	95.0	119.0	151.0

[a]The origin of the x-y coordinates is 9 m downstream from the flume inlet, along the centreline.

quoted in Table I. The spacing between the two wires was 13 mm for the longitudinal array and 10 mm for the transverse array.

The conductance wave probes were calibrated in stationary water at 6 depths from 30 mm to 130 mm. The average voltage output was measured at each depth and the line of best fit was applied to the data to determine the calibration function for each probe. The average calibration sensitivity of the probes was of the order of 10 mm/V. The elevation time-series were recorded through a set of Churchill Controls WM1A wave monitors and digitized by a National Instrument PXIe acquisition board. The data acquisition system had an accuracy of 0.3 mV that corresponded to a 0.003 mm vertical resolution. The wave probe recordings in still water were characterised by a very slow unsteady drift in time (less than 10^{-2} mm over 10 s). As a result, the rms noise level estimated from 10 min measurements was approximately 0.05 mm, which was reduced below 0.01 mm by band-pass filtering the signal with a second-order Butterworth filter between the frequencies 0.1 Hz and 20 Hz.

Each measurement lasted for 10 min. The sampling frequency was 500 Hz. The maximum frequency of the waves which the waveprobes were able to resolve was estimated as $\omega(k_{s,x}/2,0)/2\pi = 16.6$ Hz, where $k_{s,x}$ was the Nyquist wavenumber which is determined in Sec. III. $\omega(k_{s,x}/2,0)$ was calculated from the dispersion relation of gravity waves in an irrotational flow (Equations (12) and (10)), in the conditions where the Doppler shift due to the current was maximum. The recorded data sets were therefore downsampled to an effective sampling frequency of 50 Hz after filtering.

C. Flow conditions

Thirteen different flow conditions were studied. Each flow condition was unique in terms of the uniform mean flow depth, H, and the slope, s, of the flume. These parameters are reported in Table II together with the measured mean surface velocity U_0 and the characteristic Froude and Reynolds numbers. Table II also reports the measured standard deviation of the free surface fluctuations, σ. This was determined as the average across all the probes of the streamwise array. The wavenumber of the stationary waves, k_0, expected from Equation (9) for each flow condition is also given in Table II.

The non-dimensional parameter $k_0 H/\pi$ corresponds to twice the ratio between the uniform flow depth and the wavelength of the stationary waves. In a deep irrotational flow, $k_0 H = 1/F^2$, where F is the Froude number. When k_0 is determined for the 1/3 power function profile, $k_0 H$ represents the inverse of a squared Froude number, corrected for the velocity profile of the shallow turbulent flow. In an attempt to investigate the behavior of the free surface when the Froude number changes, the different flow conditions reported in Table II were grouped based on the value of $k_0 H/\pi$. Flow conditions 2–5 had $k_0 H/\pi > 1.4$ and $F < 0.5$. They were representative of relatively deep flows. Flow conditions 10–13 had $k_0 H/\pi < 1$ and $0.61 \leq F \leq 1$, and they represented the largest Froude number flows across our measurements. Conditions 6–9 had $k_0 H/\pi$ between 1 and 1.36 and they constituted the intermediate range of Froude number in our measurements ($0.52 \leq F \leq 0.61$). The threshold values of 1 and 1.4 were chosen arbitrarily in order to give the same number of flow conditions in each group. Condition 1 had the mean surface velocity lower than the minimum phase velocity of gravity-capillary waves; therefore, the stationary waves could not exist under this flow condition and it was impossible to define k_0 based on Equation (9).

TABLE II. Test flow conditions.

Flow condition	H[a] (mm)	s[b] (-)	U_0[c] (m/s)	F[d] (-)	Re[e] (-)	σ[f] (mm)	k_0[g] (rad/m)	$k_0 H/\pi$[ ] (-)	$1/n$[h] (-)
1	42.2	0.001	0.19	0.30	8.0×10^3	0.05	…	…	2.8
2	72.9	0.001	0.35	0.41	2.5×10^4	0.40	89.7	2.08	3.3
3	101.0	0.001	0.41	0.41	4.1×10^4	0.50	63.6	2.05	3.5
4	42.2	0.002	0.30	0.47	1.3×10^4	0.25	131.5	1.77	2.8
5	101.3	0.002	0.49	0.49	4.9×10^4	1.79	45.1	1.45	3.5
6	43.0	0.003	0.34	0.52	1.5×10^4	0.49	99.7	1.36	2.8
7	73.1	0.002	0.46	0.54	3.4×10^4	1.21	52.4	1.22	3.3
8	40.5	0.004	0.36	0.57	1.5×10^4	0.34	89.5	1.15	2.8
9	43.4	0.005	0.40	0.61	1.7×10^4	0.46	72.6	1.00	2.8
10	99.0	0.003	0.60	0.61	5.9×10^4	2.03	31.4	0.99	3.5
11	72.4	0.003	0.54	0.64	3.9×10^4	1.17	39.4	0.91	3.3
12	43.1	0.006	0.43	0.66	1.8×10^4	0.57	63.8	0.88	2.8
13	73.2	0.004	0.58	0.68	4.2×10^4	1.10	34.8	0.81	3.3

[a]H is the mean depth as measured with mechanical point gauges.

[b]s is the channel slope.

[c]U_0 is the mean surface velocity.

[d]F is the Froude number based on the mean depth and mean surface velocity, $F = U_0(gH)^{-1/2}$.

[e]Re is the Reynolds number based on the mean surface velocity and mean depth, $Re = \rho U_0 H \mu^{-1}$.

[f]σ is the mean standard deviation of the free surface elevation (average across all longitudinal probes).

[g]k_0 is the characteristic wavenumber estimated according to Equation (9).

[h]n is the exponent of the power-function velocity profile estimated according to Cheng,[24] Equations (34) and (35), with $n^{-1}\sqrt{f} = 1.0$.

III. ANALYSIS PROCEDURE

For each flow condition, the free surface elevation with respect to H, ζ, was measured simultaneously at each wave probe in the two arrays. The data were analysed separately for the streamwise and the transverse array. In this section, the analysis procedure is presented for the streamwise measurements. The extension of this procedure to the transverse array is straightforward. The standard deviation σ_ν at the νth probes was calculated as

$$\sigma_\nu^2 = \frac{1}{M} \sum_{\mu=1}^{M} [\zeta(x_\nu, t_\mu)]^2, \qquad (2)$$

where x_ν was the spatial position of the probe. The recording at each probe was sampled in time with the frequency $f_s = 1/\Delta t = 50$ Hz. The duration of each measurement was $T = M\Delta t$, and $t_\mu = \mu\Delta t$, $\mu = 1, 2, \ldots, M$ was the sampled time vector. The space-time correlation function was assumed to be independent of the position x and time t. This assumption does not hold if there are spatial patterns on the surface that are constant in time, such as stationary waves. The above limitation to the analysis was addressed by splitting the measured signal into 59 separate segments, each being 10 s long. For each of these segments, the linear trend in time was removed from the measurement. This procedure eliminated the deterministic stationary component of the free surface elevation from each time series. The resulting space time-correlation function in the direction x only depended on the spatial and temporal separations, r_n and τ_m, respectively. Each combination of two probes (ν, η) defined a temporal correlation function at the spatial separation $r_n = x_\nu - x_\eta$. All combinations of two probes (ν, η) whose spatial separation was similar and within $\pm\delta_r$ were identified, where δ_r was set equal to 5 mm. For these combinations the average separation $\bar{r}_n$ was determined, so that $N_{\bar{r}_n}$ was the number of pairs (ν, η) with $\bar{r}_n - \delta_r \leq x_\nu - x_\eta \leq \bar{r}_n + \delta_r$. The space-time correlation function was then determined as

$$W_x(\bar{r}_n, \tau_m) = \sum_{r_n \approx \bar{r}_n} \sum_{\mu=1}^{M} \frac{\zeta(x_\nu, t_\mu)\zeta(x_\eta, t_\mu - \tau_m)}{\sigma_\nu \sigma_\eta N_{\bar{r}}}. \tag{3}$$

This procedure applied to the arrays of wave probes produced $2N_x - 1 = 57$ unique separations $\bar{r}_n$ along the streamwise array, and $2N_y - 1 = 25$ unique separations along the transverse array. $N_x = 29$ and $N_y = 13$ were the number of non-negative separations for each of the arrays, respectively. The resulting set of spatial separations $\bar{r}_n$ was non-equidistant. The direct application of the discrete Fourier transform to the correlation function of Equation (3) in order to determine the frequency-wavenumber spectrum would be affected by strong spectral leakage. Donelan, Hamilton, and Hui[35] introduced a least-squares fitting procedure in the reciprocal domain to correct for the distortion caused by spectral leakage. Here an alternative iterative method where the correlation function $W_x(\bar{r}_n, \tau_m)$ was interpolated onto an equidistant set of separations $\bar{r}_e$ prior to performing the Fourier transform was adopted. The interpolation was performed by means of an iterative algorithm[36] combined with a sinc function reconstruction technique.[37,38] The details of this technique are explained in the Appendix. The result was the regularized function $\hat{W}_x(\bar{r}_e, \tau_m)$. This was defined at $2N_x - 1$ equally spaced locations $\bar{r}_e$ between $-L_x$ and L_x, with $L_x = 762.5$ mm (between $-L_y$ and L_y, with $L_y = 151.0$ mm for the transverse array), and at $2M - 1$ time separations τ_m between $-T$ and T, where $T = 10$ s. The spatial and temporal increments in the streamwise flow direction were $\Delta\bar{r}_e = 2L_x/2(N_x - 1)$ and $\Delta\tau = 2T/2(M - 1)$, respectively.

The reconstructed correlation function at 0 time lag $\hat{W}_x(\bar{r}_e, 0)$ is compared to $W_x(\bar{r}_n, 0)$ in Fig. 3 for flow condition 11. In order to eliminate the discontinuity at the boundary where the correlation function was non-zero (see Fig. 3), $\hat{W}_x(\bar{r}_e, \tau_m)^{(\kappa)}$ was multiplied by a two-dimensional Hanning window in space and time. The frequency-wavenumber spectrum was finally calculated with the standard two-dimensional discrete Fourier transform at the equidistant discrete radian frequency ω and wavenumber k_x as

$$S_x(k_x, \omega) = \sum_{m=1}^{M} \sum_{e=-N_x}^{N_x} \hat{W}_x(\bar{r}_e, \tau_m) \exp\left[i\left(k_x\bar{r}_e - \omega\tau_m\right)\right]\Delta\bar{r}_e\Delta\tau, \tag{4}$$

with the typical frequency and wavenumber resolution $\Delta\omega = 2\pi f_s/(2M - 1)$ and $\Delta k_x = 2\pi/(2N_x - 1)\Delta\bar{r}_e$, respectively. $S_x(k_x, \omega)$ was normalized such that

$$\sum_{\omega=0}^{\omega(k_{s,x}/2, 0)} \sum_{k_x=-k_{s,x}/2}^{k_{s,x}/2} S_x(k_x, \omega)\Delta k_x\Delta\omega = 1, \tag{5}$$

where the summation was carried out over both the frequency and the wavenumber axes. The frequency power spectrum was estimated from the sum
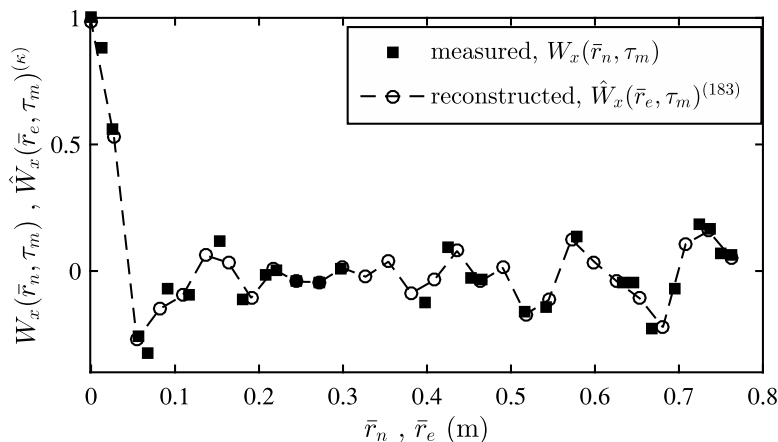

FIG. 3. An example of the correlation functions at 0 time lag, for condition 11: (squares) estimated directly, $W_x(\bar{r}_n, 0)$, (circles) reconstructed through the proposed iterative procedure at the 183-th iteration, $\hat{W}_x(\bar{r}_e, 0)^{(183)}$.

$$S_x(\omega) = \sum_{k_x=-k_{s,x}/2}^{k_{s,x}/2} S_x(k_x,\omega)\Delta k_x, \tag{6}$$

taken along the wavenumber axis only.

It should be noted that $S_x(k_x,\omega)$ and $S_x(\omega)$ were determined from the space-time correlation function in the x-direction; therefore, they depended on the projection of the wavenumber $\mathbf{k}$ in the streamwise direction, $k_x = |\mathbf{k}|\cos\theta$, which is different from $k = |\mathbf{k}|$ in general. The corresponding spectra in the transverse y-direction, $S_y(k_y,\omega)$ and $S_y(\omega)$, depended on $k_y = |\mathbf{k}|\sin\theta$ and they were found in the similar way, with the obvious change of the indices and coordinates. From the sensor arrangement reported in Table I, the spectral resolutions were $\Delta k_x = 4.05$ rad/m and $\Delta k_y = 19.95$ rad/m in the x- and y-direction, respectively. The Nyquist wavenumber k_s was governed by the average separation $\Delta\bar{r}_e$, as $2\pi/\Delta\bar{r}_e$. It was $k_{s,x} = 231$ rad/m and $k_{s,y} = 499$ rad/m for the two directions, respectively.

IV. DISPERSION RELATION OF GRAVITY-CAPILLARY WAVES ON A SHALLOW TURBULENT FLOW

The solution to the linearized boundary problem of gravity-capillary waves propagating at the surface of a shallow flow with vorticity has been derived by several authors for different relationships used to describe the shape of the vertical velocity profile.[16,17,19,39] The numerical solution proposed by Shrira[19] applies to an arbitrary shape of the velocity profile, but it has been determined for the infinite depth case only, while the solution derived by Patil and Singh[39] is valid for the logarithmic profile and for the long wavelength limit. The vertical velocity profile in a turbulent shallow flow with rough static bed can be approximated by a power law of the vertical coordinate (Equation (1)), such as the 1/7 power function considered by Fenton[17] and by Lighthill in the Appendix of the work of Burns.[16]

In this work, the same derivation reported by Fenton[17] and Lighthill[16] was adopted to study the dispersion relation for flows with the exponent $n = 1/3$. The flow was assumed to be inviscid and incompressible, with a constant uniform depth H, so that the bed roughness was neglected. The vertical coordinate z varied from $z = 0$ at the bottom to $z = H + \zeta$ at the free surface. $\zeta(x,y,t)$ was represented in terms of the trigonometric series $\zeta(x,y,t) = \sum_j Z_j e^{i(\mathbf{k_j}\cdot\mathbf{x}-\omega_j t+\psi_j)}$, where only the real part of $\zeta(x,y,t)$ must be considered. $\mathbf{k_j} = k_{x,j}\mathbf{i_x} + k_{y,j}\mathbf{i_y}$ is the wavenumber vector with magnitude $k_j = |\mathbf{k_j}| = 2\pi/\lambda_j$, where λ_j is the wavelength and ω_j is the radian frequency. ψ_j represents the phase of the jth term with amplitude Z_j.

Previous works[16,17] considered a single plane harmonic wave $\zeta(\xi,t)$ in the plane (ξ,z) parallel to $\mathbf{k_j}$ so that $\mathbf{k_j}\cdot\mathbf{i}_\xi = k_j$ and attempted to find an expression for the phase velocity $c_j(k_j) = \omega_j/k_j$. In this work, the component of the mean velocity in the direction ξ was given by $U_\xi(z) = U_0(z/H)^n\cos\theta_j$, where θ_j is the angle between the wavenumber $\mathbf{k_j}$ and the direction of the mean flow, $\mathbf{i_x}$, and U_ξ is constant along the direction ξ. The phase velocity was found by numerically integrating a first-order nonlinear Riccati equation (Equation (18) in Fenton[17]). With respect to the notation used by Fenton, $U_\xi(z)$ was written in place of $U(y)$, and the gravity constant, g, was replaced by $\tilde{g} = g + k_j^2\gamma/\rho$, where γ is the surface tension coefficient and ρ is the density of water. The integration was then performed with a fourth-order Runge-Kutta method on a grid of 100 points between $\hat{z} = 0$ and $\hat{z} = 1$, in terms of the non-dimensionalized z-dependent factor of the stream function, $p(\hat{z})$. The solution $p(1)$ at $\check{z} = 1$ was then used in order to determine the phase velocity (from now on the subscript j is omitted),

$$c^2 = \frac{Hp(1)\left(g + \frac{\gamma}{\rho}k^2\right)}{(1-\epsilon)\left[np(1)\epsilon - \epsilon + 1\right]} \tag{7}$$

for a given $\epsilon = U_0\cos\theta_j/c$. The phase velocity of the gravity-capillary waves in still water with infinite depth is

$$c_s(k) = \sqrt{\frac{g}{k} + \frac{\gamma}{\rho}k} \tag{8}$$

that has a minimum $c_{min} \approx 0.23$ m/s. In this work, the initial value problem had a singularity when the projection of the time-averaged flow velocity in the direction of the wave propagation was equal to the phase velocity of the gravity-capillary waves, i.e., $U_\xi = c$. In this case, the numerical integration was impeded. This singularity (which corresponds to the critical layer instability) was found for all waves propagating upstream with $|c_s| < U_0$. Therefore, a solution with the power function velocity profile was not attempted for these waves. The stationary waves with $c(k_0) = 0$ that propagate against the flow with $\theta = \pi$ had the wavenumber k_0 which was found analytically according to Lighthill[16] (the similar equation reported by Fenton[17] has a mistake),

$$k_0 \frac{I_{-1/2-n}(k_0 H)}{I_{1/2-n}(k_0 H)} = \frac{g + \frac{\gamma}{\rho} k_0^2}{U_0^2}, \tag{9}$$

where I_n is the modified Bessel function of order n. Equation (9) has two solutions when $U_0 \geq c_{min}$ in the range of depths which were studied in this work (between 40 mm and 100 mm). Of these, the solution with the smaller k that represents the gravity waves is of larger interest for this study.

When the velocity is constant along z, $U(z) = U_0$, the irrotational solution is found as

$$c_{irr}(k, \theta) = U_0 \cos \theta \pm c_s(k)\sqrt{\tanh kH}, \tag{10}$$

where the $\pm$ sign represents waves that can propagate in both directions parallel to the wavenumber vector **k**. The wavenumber of the stationary waves propagating against the flow with $\theta = \pi$ based on the irrotational theory, k_0^I, was found from the solution of

$$U_0 = c_s(k_0^I)\sqrt{\tanh k_0^I H}. \tag{11}$$

The dispersion relation was defined as

$$\omega(k, \theta) = kc(k, \theta), \tag{12}$$

where c was determined from Equation (7) for the 1/3 profile or from Equation (10) for the constant velocity profile, respectively. The group velocity of gravity-capillary waves, c_g, was defined as

$$c_g(k, \theta) = \frac{\partial \omega(k, \theta)}{\partial k}. \tag{13}$$

In order to quantify the difference between the proposed dispersion relations and the measured spectra, the same strategy as described by Herbert, Mordant, and Falcon[32] was implemented. The ridges of the streamwise spectra $S_x(k_x, \omega)$ were identified with a Gaussian fitting along the wavenumber k_x at each frequency ω. The maximum fit indicated the wavenumber of the measured ridges. This was then subtracted from the wavenumber predicted at the same frequency by each of the proposed relations. The root mean squared average of the difference between the two wavenumbers, defined as ε_k, was calculated separately in the frequency ranges $\omega < 2k_0 U_0$ and $\omega > 2k_0 U_0$ for both the irrotational dispersion relation (Equation (10)) and the relation with the 1/3 velocity profile (Equation (7)). These two frequency ranges were representative of the two types of surface patterns discussed in Section V B. The values of ε_k are shown in Fig. 12 and reported in Table III for all the measured flow conditions and for both the irrotational dispersion relations and the dispersion relations obtained with the 1/3 velocity profile.

TABLE III. Root mean squared average difference, ε_k, between the ridges of the measured streamwise spectra, $S_x(k_x, \omega)$, and the proposed dispersion relations, evaluated along the k_x axis. Dimensions are in rad/m.

Flow condition	1	2	3	4	5	6	7	8	9	10	11	12	13
1/3 profile, $\hat\omega < 2$	2.5	8.9	2.0	34.1	3.1	13.2	2.1	7.6	3.4	3.5	3.7	2.9	5.7
Irrotational, $\hat\omega < 2$	1.1	6.3	3.3	30.3	1.5	12.2	3.8	6.2	3.2	4.7	7.0	8.2	8.5
1/3 profile, $\hat\omega > 2$	...	2.0	5.0	...	2.0	3.5	2.7	1.9	2.1	2.8	3.2	2.4	2.8
Irrotational, $\hat\omega > 2$	5.4[a]	2.3	4.0	...	2.3	6.0	4.1	2.4	1.0	1.7	4.6	1.3	3.7

[a]Difference calculated with respect to the relation $k_x = \omega/U_0$ in the frequency range $0 < \omega U_0/g < 0.3$.
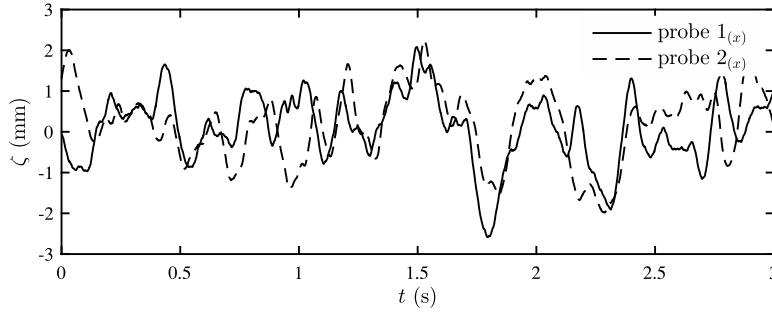
FIG. 4. An example of the time series of the free surface elevation for condition 13, before filtering and downsampling. (Solid) Probe $1_{(x)}$. (Dashed) Probe $2_{(x)}$. The mean surface velocity was $U_0 = 0.58$ m/s, and the distance between the probes was 26 mm.

V. EXPERIMENTAL RESULTS

A. The spatial and temporal scales

An example of the free surface elevation measured with two wave probes on the x-axis (probes $1(x)$ and $2(x)$) is shown in Fig. 4. The average of the standard deviation σ_ν over all probes from $1_{(x)}$ to $8_{(x)}$, σ, is shown in Table II. A clear empirical relationship that describes the dependence of σ from the flow characteristics could not be found.

Fig. 5 shows examples of the dimensional power spectral density, $\sigma^2 S_x(\omega)$, and of the spatial correlations at zero time lag, $W_x(r_x, 0)$ and $W_y(r_y, 0)$, respectively, for flow conditions 1, 4, 7, and 10. These conditions were representative of the range of spatial and temporal scales, $2\pi/k_0$ and $k_0 U_0$, respectively. In this and in the following figures, the spectra are only shown up to the frequency $\omega(k_{s,x}/2, 0)$. Fig. 5(a) shows the increase of the power spectral density at all frequencies when the Froude number increases. This pattern of behavior was not observed for all flow conditions.

Fig. 5(b) shows examples of the correlation function at zero time lag as a function of the spatial separation, for the same flow conditions. The spatial correlation function at the time lag $\tau = 0$ was representative of the instantaneous free surface topology, and it was symmetrical with respect to both $r_x = 0$ and $r_y = 0$. r_x and r_y represented the complete set of non-equidistant separations r_n in the streamwise and transverse direction, respectively. The spatial correlation function appeared to shift towards the larger values of r_x and r_y from conditions 1 and 4 to condition 7 and condition 10.

As an attempt to provide a more clear representation of the free surface behavior across the range of measurements, the radian frequency and the spatial separation were non-dimensionalized
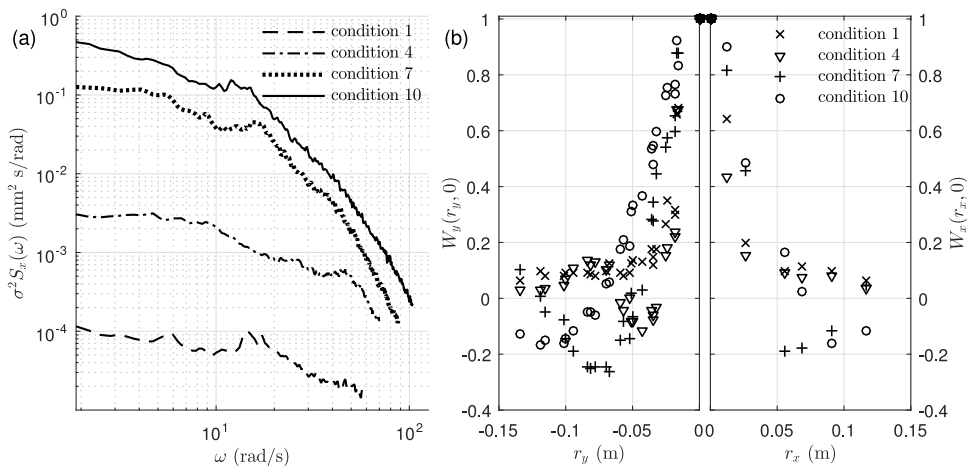

FIG. 5. (a) The dimensional frequency power spectral density $\sigma^2 S_x(\omega)$ for conditions 1, 4, 7, and 10. $S_x(\omega)$ is calculated from Equation (6). (b) The spatial correlation at zero time lag for the same flow conditions. The negative x-axis shows the transverse correlation, $W_y(r_y, 0)$, while the positive x-axis shows the streamwise correlation, $W_x(r_x, 0)$.

based on the characteristic quantities $k_0 U_0$ and $2\pi/k_0$, respectively. The choice of these parameters for the normalization derived from hypothesis (iii) that the typical spatial scale of the free surface patterns is governed by the interaction with the static rough bed, which produces the stationary waves with the wavenumber k_0. $2\pi/k_0$ is the wavelength of the stationary waves which were found from the solution of Equation (9). In condition 1, k_0 could not be defined; therefore, the non-dimensionalization for this condition was based on the quantities g/U_0 and $2\pi U_0^2/g$. The latter is the wavelength of the stationary waves determined for an infinitely deep flow if the surface tension is negligibly small.

Examples of the spatial correlation function at $\tau = 0$ along the two directions, $W_x(r_x, 0)$ and $W_y(r_y, 0)$, are given in Fig. 6 for all the investigated conditions. The correlation function for condition 1 (see Fig. 6(a)) decays monotonously and symmetrically from $r_{x,y} = 0$ in both directions. The correlation at zero time lag decays rapidly below 0.15 at $r_{x,y} g/(2\pi U_0^2) = 1.5$, which corresponds to $r_{x,y} = 35$ mm. The patterns on the free surface were isotropic and had horizontal scales comparable with the depth of the flow. The correlation function remains approximately equal to 0.1 between $r_{x,y} g/(2\pi U_0^2) = 2$ and $r_{x,y} g/(2\pi U_0^2) = 10$ ($r_{x,y} = 231$ mm), then it decays rapidly to zero.

The remaining flow conditions shown in Figs. 6(b)–6(d) display the fluctuation of $W_x(r_x, 0)$ and $W_y(r_y, 0)$ with a minimum between $r_{x,y}/(2\pi/k_0) = 0.5$ and $r_{x,y}/(2\pi/k_0) = 0.8$ and a relative maximum between $r_{x,y}/(2\pi/k_0) = 1$ and $r_{x,y}/(2\pi/k_0) = 1.6$. The smaller values are found for the higher Froude number conditions of Fig. 6(d), and the larger for the lower Froude number conditions of Fig. 6(b). The fluctuation is not observed for the streamwise correlation $W_x(r_x, 0)$ in condition 4 (Fig. 6(b)), and the minimum of the transverse correlation $W_y(r_y, 0)$ is positive in conditions 3 (Fig. 6(b)), 9 (Fig. 6(c)), and 12 (Fig. 6(d)). The spatial correlations are slightly asymmetric, and the larger negative minimum was found for the streamwise correlation $W_x(r_x, 0)$. The increased amplitude of the fluctuations of $W_x(r_x, 0)$ towards $r_x = L_x$ which can be seen in Fig. 3 relative
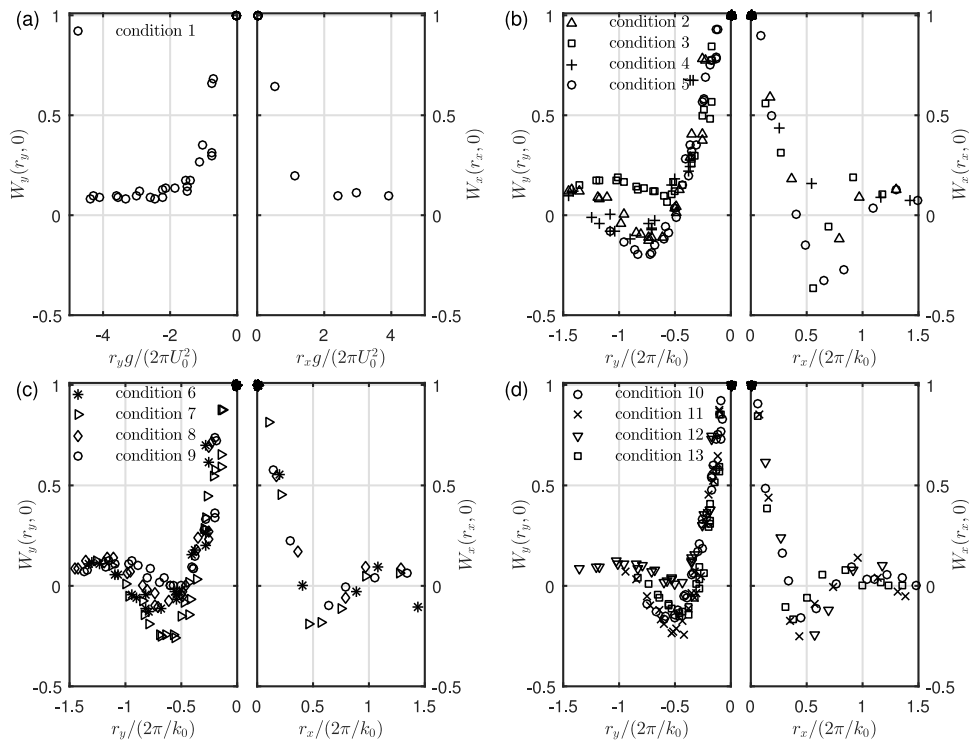

FIG. 6. The normalized spatial correlation at zero time lag, with normalized spatial separation, $r k_0/2\pi$. The negative x-axis shows the transverse correlation, $W_y(r_y, 0)$, while the positive x-axis shows the streamwise correlation, $W_x(r_x, 0)$. (a) Condition 1, (b) conditions 2–5 ($F < 0.5$), (c) conditions 6–9 ($0.52 \leq F \leq 0.61$), (d) conditions 10–13 ($0.61 \leq F \leq 0.68$). Note the different normalization in (a), where k_0 cannot be defined.

to one single realization cannot be observed from the average correlations, which remain within ± 0.1 when $r_{x,y}/(2\pi/k_0) \geq 2$ in all flow conditions, before the Hanning window was applied. The decay rate of the correlation in the region $r_{x,y}/(2\pi/k_0) \leq 0.5$ is similar in both directions, and more rapid at the higher Froude numbers. In the lower and intermediate Froude number conditions where $k_0 H/\pi > 1$ (Figs. 6(b) and 6(c)), the correlation function is equal to 0.5 at $r_{x,y}/(2\pi/k_0) \approx 0.2$. In the higher Froude number conditions where $k_0 H/\pi < 1$ (Fig. 6(d)), the value of 0.5 is attained at $r_{x,y}/(2\pi/k_0) \approx 0.15$.

Fig. 7 shows the frequency power spectra $S_x(\hat{\omega})$ and $S_y(\hat{\omega})$, calculated according to Equation (6) from the measured streamwise and transverse spectra, $S_x(k_x, \omega)$ and $S_y(k_y, \omega)$, respectively. The
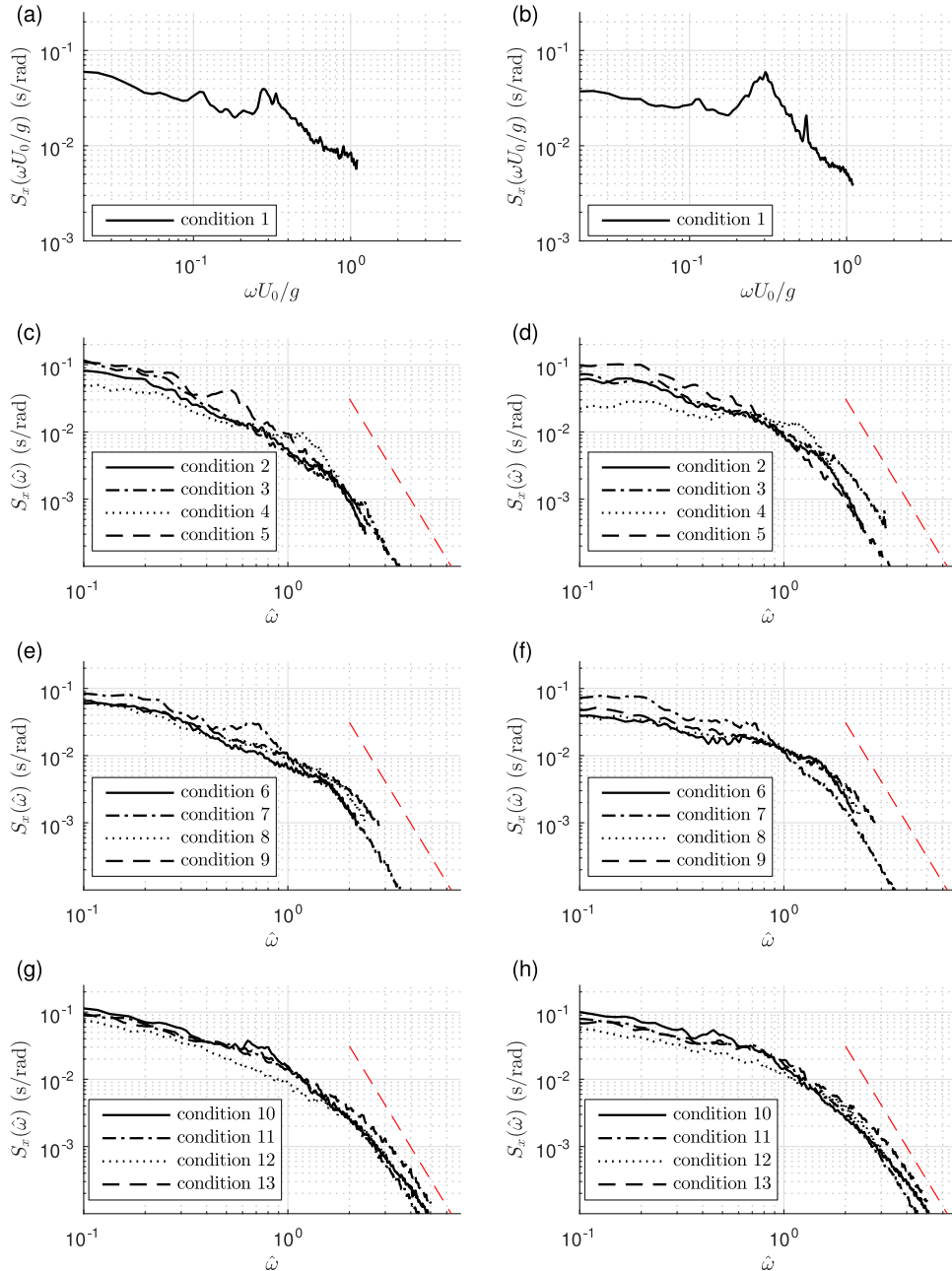

FIG. 7. The frequency power spectrum (Equation (6)) of the normalized surface elevation calculated from the streamwise spectrum $S_x(\hat{\omega})$ ((a), (c), (e), (g)), and the transverse spectrum $S_y(\hat{\omega})$ ((b), (d), (f), (h)), with the normalized frequency $\hat{\omega} = \omega/k_0 U_0$. (Dashed, red) Power decay $\propto \hat{\omega}^{-5}$, shown for reference. Note the different scaling in (a) and (b).

frequency spectra for flow condition 1 are shown in Figs. 7(a) and 7(b). Both the streamwise and the transverse spectra showed a slow decay with the frequency $\omega U_0/g$ and had one small peak near $\omega U_0/g = 0.1$ and one larger peak near $\omega U_0/g = 0.3$. The frequency spectra for the flow conditions other than condition 1 (see Figs. 7(c)-7(h)) decayed smoothly from a maximum at the frequency that tended asymptotically to $\hat{\omega} = 0$. The frequency spectra showed a similar behavior when plotted against the non-dimensional frequency $\hat{\omega}$, in each range of Froude numbers. The rate of decay of the frequency spectra of Figs. 7(c)-7(h) increased at the higher frequencies. In Figs. 7(c)-7(h), the power function law $S(\omega) \propto \hat{\omega}^{-5}$ is represented only for reference. The comparison with the measurements in Figs. 7(c)-7(h) shows that the decay of the spectra in the region $\hat{\omega} > 2$ is slower for the higher Froude number conditions (Figs. 7(g) and 7(h)) than for the lower and intermediate Froude number conditions (Figs. 7(c)-7(f)).

B. The frequency-wavenumber spectra of the free surface in two spatial dimensions

Figs. 8(a) and 8(b) show the contours for the logarithm of the dimensional streamwise and transverse frequency-wavenumber spectra $\log_{10}\sigma^2 S_x(k_x,\omega)$ and $\log_{10}\sigma^2 S_y(k_y,\omega)$, respectively, for flow condition 13. Four contours are plotted in Figs. 8(a) and 8(b) for each order of magnitude. In order to improve the visualization at the higher frequencies, Figs. 8(c) and 8(d) also show the colormaps for the corresponding normalized frequency-wavenumber spectra $S_x(\hat{k}_x,\hat{\omega})/(S_x(\hat{\omega})/k_{s,x})$ and $S_y(\hat{k}_y,\hat{\omega})/(S_y(\hat{\omega})/k_{s,y})$. The colors in Figs. 8(c) and 8(d) are on a linear scale. The non-dimensionalized frequency and wavenumber axes in Figs. 8(c) and 8(d) were defined as $\hat{\omega} = \omega/k_0 U_0$ and $\hat{k} = k/k_0$, respectively. The negative $\hat{k}_x$ represents the solution where $c < 0$, i.e., the waves that travel upstream in the laboratory frame of reference. The dimensional spectra show clear ridges in which the width is constant and comparable to the spectral resolution Δk_x and Δk_y in Figs. 8(a) and
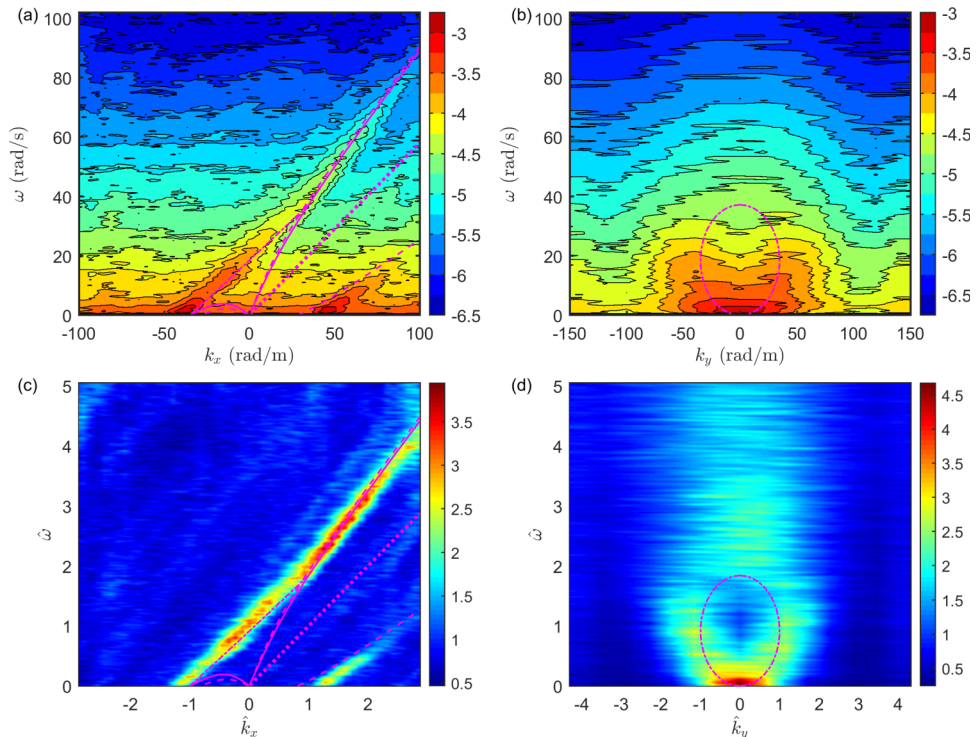

FIG. 8. (a) Contour plot of the dimensional frequency-wavenumber spectrum for condition 13, $\log_{10}(\sigma^2 S_x(k_x,\omega))$, (b) transverse spectrum $\log_{10}(\sigma^2 S_y(k_y,\omega))$. (c) The normalized frequency-wavenumber spectrum, $S_x(\hat{k}_x,\hat{\omega})/(S_x(\hat{\omega})/k_{s,x})$, (d) normalized transverse frequency-wavenumber spectrum $S_y(\hat{k}_y,\hat{\omega})/(S_y(\hat{\omega})/k_{s,y})$. (Dashed) Irrotational dispersion relation, Equation (10). (Solid) Dispersion relation with the 1/3 velocity profile, Equation (7), with $\theta = 0$. (Dotted) Non-dispersive relation, $\omega = k_x U_0$. (Dashed-dotted) Dispersion relation with the 1/3 velocity profile, Equation (7), with constant $k = k_0$.

8(b), respectively. Away from the ridges, the spectra show a noise floor which is almost constant at the same frequency, and it is a consequence of measuring with a non-equidistant array of sensors. The amplitude of the ridges is between 2 and 7 times the noise amplitude at each frequency. The noise floor appears constant across the whole normalized spectrum, with the level ≈ 1 in Figs. 8(c) and 8(d).

In the region where $\hat{\omega} \geq 2$, the streamwise spectrum $S_x(\hat{k}_x, \hat{\omega})$ in Fig. 8(c) shows a ridge which extends from $\hat{k}_x \approx 1$ to $\hat{k}_x \approx 3$. This ridge was compared with two dispersion relations, based on Equation (12). In the first relation, the phase velocity c was determined from the irrotational solution of Equation (10). In the second relation, c was found from the solution of Equation (7) for the 1/3 velocity profile. The ridge of the transverse spectrum $S_y(\hat{k}_y, \hat{\omega})$ of Fig. 8(d) in the same frequency range, $\hat{\omega} \geq 2$, has $\hat{k}_y \approx 0$. Therefore in both relations it was assumed that the waves propagate in the positive x-direction, but only parallel to the flow velocity (i.e., $\theta = 0$ and $k = |k_x|$). The free surface pattern in the region with $\hat{\omega} > 2$ corresponded to gravity waves which propagated downstream, parallel to the mean flow.

The region of the spectrum in Fig. 8(c) for which $-1 < \hat{k}_x < 1$ is characterized by a ridge that closely follows a straight line connecting the point $\hat{k}_x = -1$, $\hat{\omega} = 0$ with the point $\hat{k}_x = 1$, $\hat{\omega} = 2$ and crossing the ordinate axis at $\hat{\omega} = 1$. The wavenumber of the stationary waves corresponds to the intersection of the dispersion relations with the abscissa axis. This was estimated from Equation (9) for the 1/3 velocity profile and from Equation (11) for the irrotational flow, giving $k_0 = 34.8$ rad/m and $k_0^I = 27.1$ rad/m, respectively. In condition 13, the intersection of the spectral ridge with the axis $\hat{\omega} = 0$ in Fig. 8(c) occurs at $k_x \approx -40$ rad/m ($\hat{k}_x \approx -1.15$). The difference between the measured wavenumber of the stationary waves and that predicted by Equation (9) was thus very close to the resolution of the spectra, $\Delta k_x = 4.05$ rad/m. The stationary waves also correspond to the maximum of the dimensional frequency-wavenumber spectrum in Fig. 8(a). The dashed-dotted lines in Figs. 8(c) and 8(d), were found by assuming a radial isotropic distribution of waves with the wavenumber k_0, propagating in all directions. The corresponding dispersion relation was the solution of Equations (7) and (12), where $k_x = k_0 \cos \theta$, $k_y = k_0 \sin \theta$, $U_\xi(z) = U_0(z/H)^n \cos \theta$, and θ was allowed to vary between 0 and π. This relation approximates the curved ridges in the region $\hat{\omega} \leq 1$ in Fig. 8(d) and the straight ridge between $\hat{k}_x = -1$ and $\hat{k}_x = 1$ in Fig. 8(c).

The proposed dispersion relations slightly underestimate the frequency of the measured spectrum in the region $-1 < \hat{k}_x < 1$ of Fig. 8(c) and overestimate it in the region $\hat{k}_x > 2$. These differences were comparable to the resolution of the spectrum, and they were caused by the uncertainty of the surface velocity measurements. The root mean squared average wavenumber difference between the maxima of the spectrum and the proposed relations was $\varepsilon_k = 5.7$ rad/m in the region $\hat{\omega} < 2$ and $\varepsilon_k = 2.8$ rad/m in the region $\hat{\omega} > 2$ (see Table III). ε_k changed to $\varepsilon_k = 4.5$ rad/m where $\hat{\omega} < 2$ and to $\varepsilon_k = 3.2$ rad/m where $\hat{\omega} > 2$, respectively, if the mean surface velocity was reduced from 0.58 m/s to 0.56 m/s, which was within the measurement uncertainty.

The part of the frequency-wavenumber spectrum in Fig. 8(c) for which $\hat{k}_x > 1$ shows an additional ridge at the frequencies $\hat{\omega} < 2$. This ridge extends from $\hat{k}_x \approx 1$ and $\hat{\omega} = 0$ to $\hat{k}_x \approx 2.5$, where $\hat{\omega} \approx 1$. The first point corresponds to the condition of stationary waves. The spectrum is compared with the dispersion relation of gravity-capillary waves propagating parallel to the flow velocity, but this time with the direction opposite to that of the flow, i.e., with $\theta = \pi$ and $k = |k_x|$. Although this relation (which is irrotational) overestimates slightly the frequency in this range, it approximates well the ridge with $\hat{k}_x > 1$ in Fig. 8(c). This suggests that these waves propagated against the flow with the phase velocity in still water (Equation (8)) slower than U_0, so that they were advected downstream with $0 < c < U_0$. In this way, they differed from the radial waves described earlier in which the phase velocity could be negative. Fig. 8(c) shows that these two types of waves occupy the same range of frequencies. In Fig. 8(d), only one type of wave (with the two curved ridges that follow the dashed-dotted lines) is clearly recognizable in the same frequency range. From the observation of the two separate spectra $S_x(\hat{k}_x, \hat{\omega})$ and $S_y(\hat{k}_y, \hat{\omega})$ in Figs. 8(c) and 8(d), it is not possible to say whether or not these ridges should also be attributed to the waves with $0 < c < U_0$. These slowly propagating two-dimensional waves were observed in flow condition 3 and in conditions 10–13 with the higher Froude number, but they were not clearly recognizable in the remaining intermediate conditions. It is likely that this was caused by the limited spatial
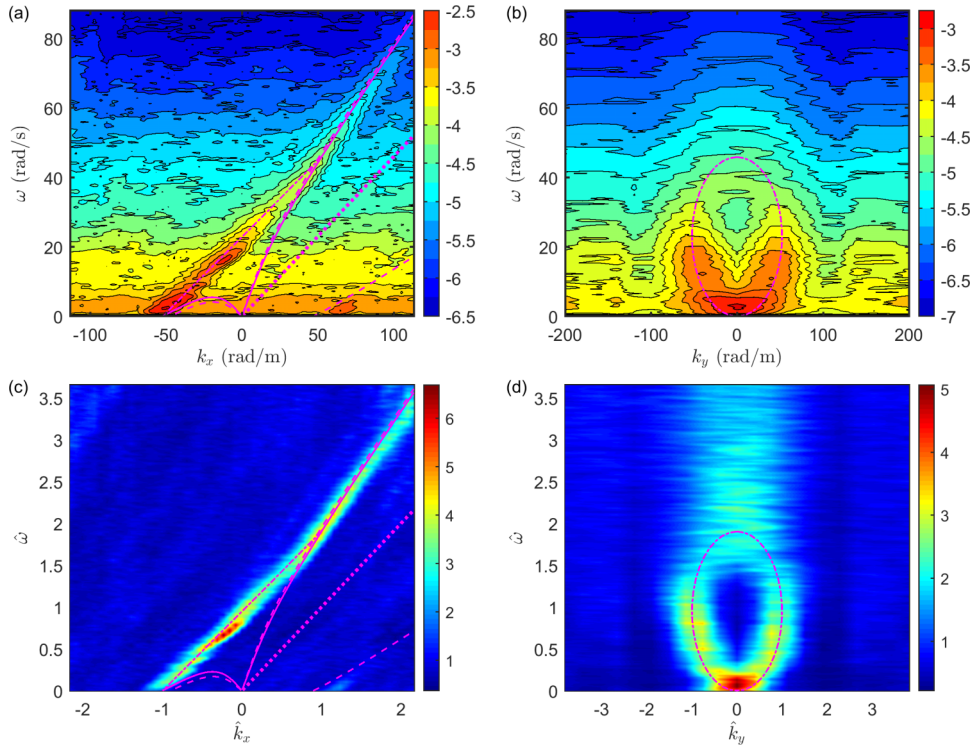
FIG. 9. (a) Contour plot of the dimensional frequency-wavenumber spectrum for condition 7, $\log_{10}(\sigma^2 S_x(k_x, \omega))$, (b) transverse spectrum $\log_{10}(\sigma^2 S_y(k_y, \omega))$. (c) The normalized frequency-wavenumber spectrum, $S_x(\hat{k}_x, \hat{\omega})/(S_x(\hat{\omega})/k_{s,x})$, (d) normalized transverse frequency-wavenumber spectrum $S_y(\hat{k}_y, \hat{\omega})/(S_y(\hat{\omega})/k_{s,y})$. (Dashed) Irrotational dispersion relation, Equation (10). (Solid) Dispersion relation with the 1/3 velocity profile, Equation (7), with $\theta = 0$. (Dotted) Non-dispersive relation, $\omega = k_x U_0$. (Dashed-dotted) Dispersion relation with the 1/3 velocity profile, Equation (7), with constant $k = k_0$.

resolution of the adopted array of waveprobes. Because of these limitations, the Gaussian fitting was not applied in this region of the spectrum.

The data for the intermediate Froude number flow conditions show a similar behavior to the case which was described in the previous paragraphs. Figs. 9(a) and 9(b) show the dimensional frequency-wavenumber spectra for flow condition 7. Figs. 9(c) and 9(d) show the corresponding normalized spectra. The spectra in Fig. 9 show the same ridges as in Fig. 8. The slow upstream waves advected downstream with the positive wavenumber and low frequency are less clear from the streamwise spectrum in Fig. 9(c) than those visible in Fig. 8(c). This is attributed to the limited spatial resolution of the measurements. The maximum of the spectrum of Fig. 9(a) is at the frequency $\omega \approx 0$ and the wavenumber $k_x = \pm 60$ rad/m, which compares well with the wavenumber of the stationary waves, $k_0 = 52.4$ rad/m. The agreement with the dispersion relation of the radial pattern in the frequency range $0 \leq \hat{\omega} \leq 2$ in Figs. 9(c) and 9(d) is better than in Figs. 8(c) and 8(d), with $\varepsilon_k = 2.1$ rad/m in the region $\hat{\omega} < 2$ and $\varepsilon_k = 2.7$ rad/m in the region $\hat{\omega} > 2$.

The pattern of the measured frequency-wavenumber spectra was consistent for all the tested flow conditions, with the exception of conditions 1 and 4. The former requires a separate discussion because the mean surface velocity $U_0 < c_{min}$ did not allow for the formation of stationary waves. The frequency-wavenumber spectra for flow condition 4 are shown in Fig. 10. In this condition, the dispersion relation with the 1/3 velocity profile predicts the wavelength of the stationary waves equal to $2\pi/k_0 = 47.8$ mm, which is comparable to the shortest waves that could be accurately measured by the streamwise array, where $k_0 \Delta r_e/(2\pi) = 0.55$. The streamwise frequency-wavenumber spectrum in Fig. 10(c) shows a cloud of points enclosed within the region of $\hat{k}_x \approx -0.8$ and $0 \leq \hat{\omega} \leq 0.5$. This was caused by the limited spatial resolution of the array. There is a ridge that corresponds to the gravity waves propagating downstream, which extends from $\hat{k}_x \approx 0.4$ to $\hat{k}_x = 0.9$ and from $\hat{\omega} \approx 1$ to $\hat{\omega} \approx 1.8$, hence $k_x < k_0$. There is a second ridge that goes from $\hat{k}_x \approx -0.2$ to $\hat{k}_x \approx 0.3$ and
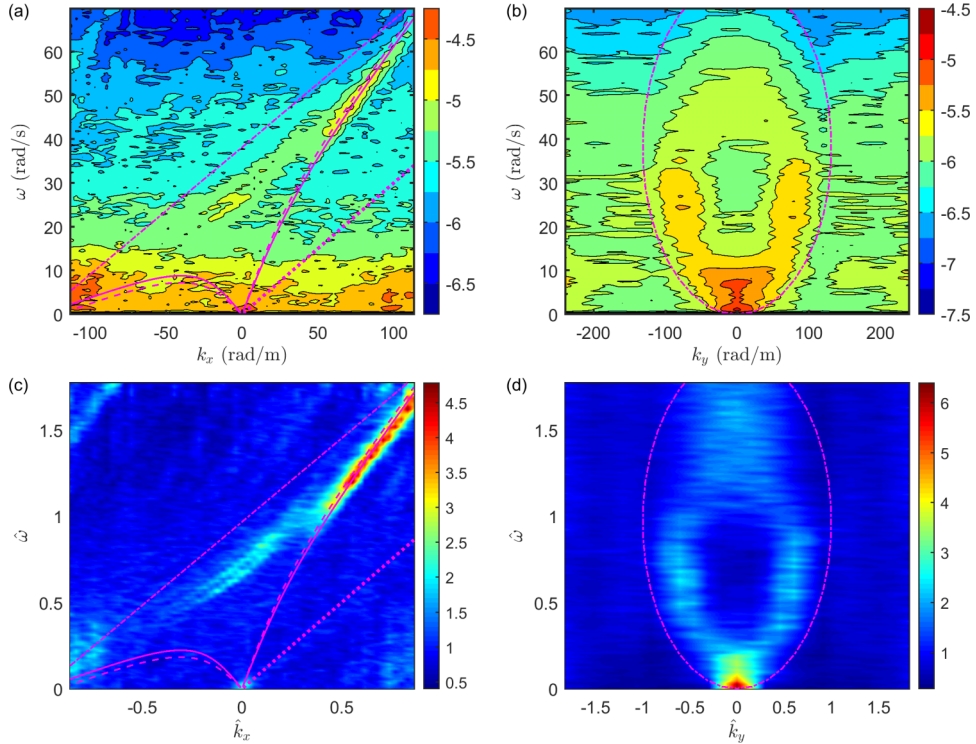
FIG. 10. (a) Contour plot of the dimensional frequency-wavenumber spectrum for condition 4, $\log_{10}(\sigma^2 S_x(k_x, \omega))$, (b) transverse spectrum $\log_{10}(\sigma^2 S_y(k_y, \omega))$. (c) The normalized frequency-wavenumber spectrum, $S_x(\hat{k}_x, \hat{\omega})/(S_x(\hat{\omega})/k_{s,x})$, (d) normalized transverse frequency-wavenumber spectrum $S_y(\hat{k}_y, \hat{\omega})/(S_y(\hat{\omega})/k_{s,y})$. (Dashed) Irrotational dispersion relation, Equation (10). (Solid) Dispersion relation with the 1/3 velocity profile, Equation (7), with $\theta = 0$. (Dotted) Non-dispersive relation, $\omega = k_x U_0$. (Dashed-dotted) Dispersion relation with the 1/3 velocity profile, Equation (7), with constant $k = k_0$.

from $\hat{\omega} \approx 0.5$ to $\hat{\omega} \approx 1.2$, but this is strongly curved and it does not follow the prediction based on the radial pattern with the constant modulus of the wavenumber $k = k_0$. The root mean squared average wavenumber difference between the maxima of the spectrum and the proposed relations was $\varepsilon_k = 34.1$ rad/m, estimated between $\hat{\omega} = 0$ and $\hat{\omega} = 2$. The transverse spectrum shown in Fig. 10(d) has a similar behavior to that of the flow conditions discussed so far, but the region where $\hat{k}_y \neq 0$ is within $0.2 \leq \hat{\omega} \leq 1.3$, and the maximum transverse wavenumber is $\hat{k}_y \approx 0.6$. These observations suggest that the radial pattern of waves had the modulus of the wavenumber smaller than k_0. The curved ridge in Fig. 10(a) suggests that the pattern was not axially symmetric, i.e., that the waves propagating parallel to the streamwise direction had the larger wavenumber (were shorter) than those propagating perpendicularly to it. The reasons for the different behavior in condition 4 are not clear and warrant further investigation.

The flow in condition 1 had the mean surface velocity U_0 which was smaller than the minimum of the phase velocity in still water, $c_{min} \approx 0.23$ m/s. Therefore the stationary waves which otherwise would dominate the free surface could not form. Figs. 11(c) and 11(d) show the normalized frequency-wavenumber spectra for condition 1 as the function of the non-dimensional wavenumber $k U_0^2/g$ and the non-dimensional frequency $\omega U_0/g$. The streamwise frequency-wavenumber spectrum is shown in Figs. 11(a) and 11(c). It shows a ridge that follows closely the dispersion relation of Equation (7) with $\theta = 0$. The agreement with Equation (7) was quantified by $\varepsilon_k = 2.5$ rad/m. The behavior was similar to that observed in the other flow conditions, but the ridge in the spectrum for condition 1 extends to the lower frequency $\omega U_0/g = 0$, and the maximum of the spectra is near $k_x U_0^2/g = 0$. On the other hand, the ridge which was attributed to the waves with the constant wavenumber $k = k_0$ propagating radially is absent in the spectrum obtained for condition 1, which confirms that the observed radial pattern was related to the stationary condition. There is a new ridge which was not noticed in the spectra for the other conditions and which follows approximately
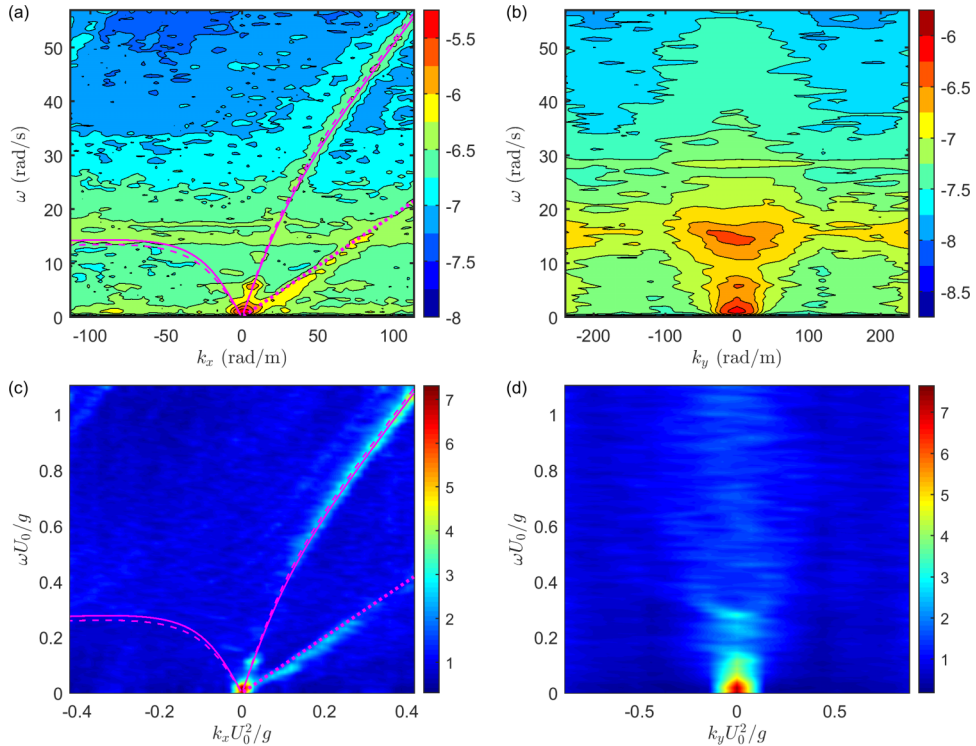
FIG. 11. (a) Contour plot of the dimensional frequency-wavenumber spectrum for condition 1, $\log_{10}(\sigma^2 S_x(k_x, \omega))$, (b) transverse spectrum $\log_{10}(\sigma^2 S_y(k_y, \omega))$. (c) The normalized frequency-wavenumber spectrum, $S_x(k_x U_0^2/g, \omega U_0/g)/(S_x(\omega U_0/g)/k_{s,x})$, (d) normalized transverse frequency-wavenumber spectrum $S_y(k_y U_0^2/g, \omega U_0/g)/(S_y(\omega U_0/g)/k_{s,y})$. (Dashed) Irrotational dispersion relation, Equation (10). (Solid) Dispersion relation with the 1/3 velocity profile, Equation (7), with $\theta = 0$. (Dotted) Non-dispersive relation, $\omega = k_x U_0$.

the non-dispersive linear relation $\omega U_0/g = k_x U_0^2/g$. In Fig. 11(c), this ridge extends from the origin of the spectrum to the point with $k_x U_0^2/g = 0.3$ and $\omega U_0/g = 0.3$, after which it becomes less clear because of the limited resolution of the measurements. The transverse spectrum in Fig. 11(d) shows a clear ridge with $k_y U_0^2/g = 0$ where $0 \le \omega U_0/g \le 0.2$, but it also becomes less clear at the higher frequency. The non-dispersive ridge in Fig. 11(a) has the amplitude 2–3 times larger than the dispersive ridge at each value of the wavenumber. The root mean squared difference between the relation $k_x = \omega/U_0$ and the wavenumber of the ridge obtained from the Gaussian fitting was $\varepsilon_k = 5.4$ rad/m, evaluated in the range $0 < \omega U_0/g < 0.3$. The frequency spectra of flow condition 1 shown in Figs. 7(a) and 7(b) have a peak at the frequency $\omega U_0/g \approx 0.3$ ($\omega \approx 15$ rad/s). At the same frequency, the streamwise spectrum of Fig. 11(a) shows a horizontal ridge spanning the whole wavenumber range, while the transverse spectrum of Fig. 11(b) has a peak at $k_y \approx 0$.

VI. DISCUSSION

The most important result of this study was the observation of the dispersion relation of the free surface patterns in turbulent shallow flows with a rough static bed. With respect to the experiments of Savelsberg and van de Water,[11] which focused on grid-generated turbulence and relatively short waves, the dispersion relation has been determined near the largest scales where the interaction with the bed manifests itself more clearly. The measurements have been compared with the dispersion relation of gravity-capillary waves in a flow with a 1/3 power function velocity profile and with the standard irrotational theory of gravity-capillary waves. The difference between the two dispersion relations and the measured spectra has been quantified with the Gaussian fitting of the ridges of the streamwise spectra, $S_x(k_x, \omega)$. The root mean squared wavenumber difference, ε_k, is shown in
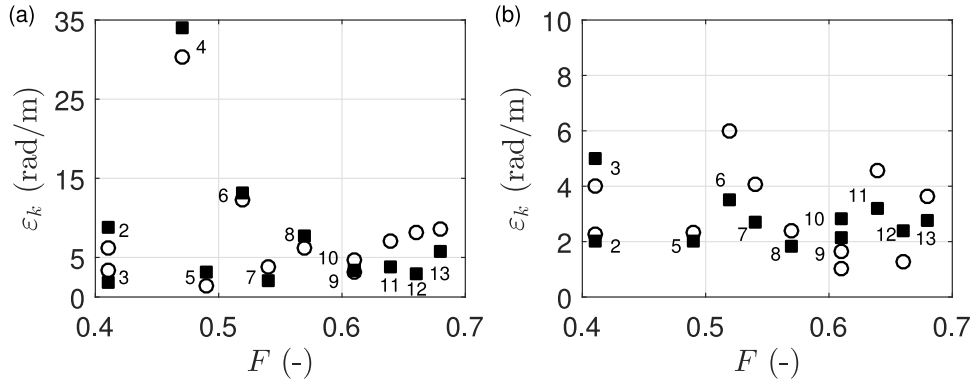
FIG. 12. Root mean squared average difference, ε_k, between the ridges of the measured streamwise spectra, $S_x(k_x, \omega)$, and the proposed dispersion relations, evaluated along the k_x axis in the interval (a) $\hat{\omega} < 2$, (b) $\hat{\omega} > 2$. (Squares) Dispersion relation with the 1/3 velocity profile. (Circles) Irrotational dispersion relation. The numbers indicate the flow conditions. The spectral resolution of the spectrum is $\Delta k_x = 4.05$ rad/m.

Fig. 12 and its values are reported in Table III for all conditions. In most flow conditions, the two theories gave very similar results, close to the resolution of the spectra. In the conditions with larger Froude number, the relation based on the 1/3 velocity profile was more accurate in the region $\hat{\omega} < 2$, where most of the amplitude of the spectrum was concentrated.

The dispersion relation based on the 1/3 velocity profile was less accurate in conditions 2, 4, 6, and 8. Of these, conditions 4, 6, and 8 had the lower mean depth of approximately 40 mm, and the smaller Froude number $F < 0.6$. Condition 4 showed a very different pattern from all other conditions, which was not fully understood. It is expected that when the submergence H/d becomes very small, the free surface would follow the shape of the boundary and the linearized equations would not be valid. It is suggested that the proposed dispersion relations become less accurate when the flow is more shallow and the Froude number is relatively low, as a consequence of either the change of the velocity profile and/or the reduced validity of the linearization of the surface equations. The results reported here support hypothesis (i), that the dispersion relation of the free surface of a shallow turbulent flow with homogeneous static bed roughness can be predicted by including the velocity profile in the derivation of the linearized equations, although further investigations would be needed in order to clarify the observed behaviour.

In all conditions with $U_0 > c_{min}$ (see Figs. 8–10), the maxima of the frequency-wavenumber spectra lie near $k_x = \pm k_0$, showing that the stationary waves represented the dominant pattern on the free surface. Patterns of waves which propagate radially in all directions, resembling the model of concentric gravity waves being shed by vertical vortices suggested by Savelsberg and van de Water,[11] were also observed. In the measurements reported here, the scale of the pattern was governed by the wavelength of the stationary waves rather than by the scale of the attached vortices. An exception was represented by condition 4, where the radial waves were shorter than the stationary waves, and the pattern was non-isotropic. Further investigations are needed in order to clarify the reasons for the different behavior at this flow condition.

The measurements of the zero-lag correlation function of the free surface elevation (Fig. 6) showed a fluctuation with the period of approximately $2\pi/k_0$, which is the typical scale of the stationary waves. In flow condition 1, the stationary waves cannot form, and the correlation function does not fluctuate. Savelsberg and van de Water[11] and Horoshenkov et al.[40] associated the decay rate and the period of the correlation function of the free surface elevation with the characteristic scales of turbulence, although Horoshenkov et al.[40] looked at the maxima in the time correlation function at each spatial separation, rather than at the zero-lag correlation at $\tau = 0$. Savelsberg and van de Water[11] and Horoshenkov et al.[40] found a correspondence between the scales of the correlation and the characteristic integral scales of turbulence. Savelsberg and van de Water[11] also observed that the correlation function becomes anisotropic when the turbulence in the flow is also anisotropic. The measurements presented here showed that when the mean surface velocity was larger than the

minimum phase velocity of gravity-capillary waves, the stationary waves rather than the turbulent scales determined the dominant scales of the free surface. This was in agreement with hypothesis (iii). The Froude number also seemed to affect the spatial characteristics of the free surface. In fact, the period of the correlation function relative to $2\pi/k_0$ and the spatial rate of decay tended to decrease when $k_0 H/\pi$ also decreased.

These observations are supported by the frequency spectra shown in Fig. 7. The shape of the frequency spectra was governed by the temporal scale $k_0 U_0$, showing that the dynamic behavior of the free surface was linked to the characteristic scales of the stationary waves. The frequency spectra decayed less rapidly at the larger frequencies when $k_0 H/\pi < 1$ and the Froude number was larger. This indicates that more energy was found in the relatively shorter and faster waves when the Froude number increased, in agreement with the progressive shift of the spatial correlation function. Smolentsev and Miraghaie[8] also observed the increase of the frequency spectrum at the higher frequencies when the Froude number increased and related this effect to the interaction with turbulence. The decrease of the slope of the spectrum resulted in an increase of the first- and second-order spatial gradients of the free surface elevation, hence it was associated with a rougher water surface. This supports hypothesis (iv) that the increase of the Froude number causes the water surface to become more rough.

The flow in condition 1 had the mean surface velocity U_0 which was smaller than the minimum of the phase velocity in still water, $c_{min} \approx 0.23$ m/s. Therefore the stationary waves which otherwise would dominate the free surface could not form. In this condition, a markedly different behavior of the correlation function and of the spectra has been observed. In condition 1, the spatial correlation function (see Fig. 6(a)) did not display a fluctuating behavior. Conversely, the frequency spectrum (see Figs. 7(a) and 7(b)) displayed a peak at the non-dimensional frequency $\omega U_0/g \approx 0.3$. The latter peak corresponds to the dimensional frequency of 2.5 Hz, which is approximately the solution of $\partial\omega/\partial k = 0$ based on Equation (13), where $\theta = \pi$. Kitaigordskii *et al.*[41] showed that the frequency spectrum $S(\omega)$ and the wavenumber angular spectrum $S(k,\theta)$ are related by

$$S(\omega) = \iint \frac{S(k,\theta)k}{\partial\Omega/\partial k}\delta\left(k - K(\omega,\theta)\right)dkd\theta, \tag{14}$$

where $K(\omega,\theta)$ represents the wavenumbers that satisfy the dispersion relation $\Omega(k,\theta)$ at the frequency ω, i.e., $\Omega(K(\omega,\theta),\theta) = \omega$. The integral of Equation (14) can become very large if the group velocity is small, which is possible for waves propagating against the flow. The peak of the frequency spectrum in Figs. 7(a) and 7(b) near the frequency where $\partial\omega/\partial k = 0$ can be justified by the existence of waves propagating upstream in flow condition 1.

The difference between condition 1 and the other conditions where $U_0 > c_{min}$ is evident from the frequency-wavenumber spectra shown in Fig. 11. These spectra still show a ridge that represents gravity waves propagating downstream, but the ridge extends to very low frequencies. This signified the existence of long waves with the wavelength comparable to the length of the array of probes, whereas in the other conditions the longest waves had the wavelength $2\pi/k_0$. The presence of the dispersive ridge in the spectrum of Figs. 11(a) and 11(c) shows that the gravity waves propagating downstream were not related to the stationary waves, which could not form in condition 1. These dispersive waves could be transient waves generated by the rough boundary or freely propagating gravity-capillary waves that originated from turbulence forced waves after the forcing has ended (e.g., because of the loss of coherence of the turbulent structures as they interact with the sheared flow near the surface,[20] or because the spatial scale of these waves is within the dissipative range of turbulence[21]). The same spectra of Figs. 11(a) and 11(c) reveal one additional set of waves which follow the non-dispersive relation $\omega = k_x U_0$. This non-dispersive ridge is believed to represent random patterns on the surface with a broad spatial spectrum, which were advected by the flow at the constant velocity U_0. These patterns are dominating over the dispersive freely propagating gravity waves at each value of the wavenumber. Teixeira and Belcher[20] have suggested that the direct interaction with turbulence is able to produce patterns of forced waves on the free surface, even when the conditions for the resonant interaction are not met. These waves are expected to follow the dispersion relation of the turbulence inside the flow, which, as a first approximation, corresponds to the non-dispersive relation $\omega = k_x U_0$. This has been observed in Figs. 11(a) and 11(c). The

results of this study provide limited evidence to support the turbulence forcing mechanism described by Teixeira and Belcher,[20] which corresponds to hypothesis (ii). More detailed hydrodynamic measurements are needed to confirm a direct link with turbulence.

VII. CONCLUSIONS

The frequency-wavenumber spectra of the free surface fluctuations in a shallow turbulent flow have been compared with a model of small amplitude waves in a rotational flow with the 1/3 power function velocity profile. The model was originally proposed by Lighthill[14] and improved by Fenton.[17] It represents an improvement with respect to the irrotational theory at the larger Froude number, and it matches the experimental results with an uncertainty comparable to the resolution of the measurements (see Fig. 12), in accordance with hypothesis (i). The deviation which was observed at the smaller depths and Froude numbers suggests that the accuracy of the model could decrease for very shallow flows.

The results reported here show that the dominant patterns on the free surface are caused by the interaction with the rough static bed when $U_0 > c_{min}$. The direct link between the scales and the statistics of the turbulence and of the free surface, which was proven experimentally[11,40] and numerically,[21,22] may become secondary due to the dominant effect of the bed roughness in many practical applications. When the mean surface velocity of the flow is larger than the minimum phase velocity of the gravity-capillary waves, $c_{min} = 0.23$ m/s, the typical spatial and temporal scales of the free surface are governed by the wavelength of the stationary waves, $2\pi/k_0$. The correlation function at zero time lag fluctuates with the period of approximately $2\pi/k_0$, as shown in Fig. 6. The shape of the frequency spectrum is governed by the characteristic frequency $k_0 U_0$, as shown in Fig. 7. The maximum of the frequency-wavenumber spectrum is found at the wavenumber $\pm k_0$ (Figs. 8–10). These results prove hypothesis (iii), that the spatial and temporal scales of the free surface can be predicted based on the wavelength of the stationary waves.

The Froude number (or the related parameter $k_0 H$) also affects the patterns of the free surface, although less strongly. When the Froude number increases, the period of the correlation function increases relative to $2\pi/k_0$ (see Fig. 6), and the frequency spectra decay less rapidly at the frequencies larger than $2k_0 U_0$ (see Fig. 7). Both effects are associated with a larger contribution from the shorter waves, which indicates a relatively rougher water surface. These observations agree with the classification of turbulent free surface flows proposed by Brocchini and Peregrine[6] and were also observed and linked to the interaction with turbulence by Smolentsev and Miraghaie.[8] They support hypothesis (iv).

In the flow condition where the mean surface velocity was slower than 0.23 m/s, the free surface was dominated by patterns moving at a velocity close to the mean surface velocity. These patterns may be explained by the interaction with coherent turbulent structures in the flow according to the model of Teixeira and Belcher.[20] The results presented here provide limited evidence to support the existence of such a mechanism, which corresponds to hypothesis (ii). It is postulated that the observed non-dispersive waves may be present in most flow conditions, although the limited spatial resolution of the arrays of wave probes in the current study and the smaller amplitude compared to the dominant stationary waves did not allow measuring them in the conditions when $U_0 > c_{min}$. This work is of importance for the development of novel, airborne instrumentation for the non-invasive characterization of the hydraulic processes in shallow water flows such as in the case of natural rivers and floods.

APPENDIX: INTERPOLATION OF THE CORRELATION FUNCTION

The adopted interpolation method used the sinc function,

$$\text{sinc}(r) = \frac{\sin(\pi r)}{\pi r}, \tag{A1}$$

as a weighing kernel defined on the single dimension r for each value of τ_m. The sinc kernel gives more accurate results than the Lomb-Scargle periodogram for non-uniformly sampled signals with harmonic components[42] and it defines a valid estimator of the correlation function.[37] In this work, an iterative algorithm[36] was added to the sinc interpolation method[37,38] to further minimize the leakage due to non-orthonormality of the sinc coefficients for the irregular set of probe separations. At the first iteration, the interpolation $\hat{W}_x(\bar{r}_e, \tau_m)^{(1)}$ of $W_x(\bar{r}_n, \tau_m)$ was calculated as

$$\hat{W}_x(\bar{r}_e, \tau_m)^{(1)} = \sum_{n=-N_x+1}^{N_x-1} W_x(\bar{r}_n, \tau_m)\text{sinc}\left[\frac{2(\bar{r}_e - \bar{r}_n)}{\Gamma\Delta\bar{r}_e}\right], \tag{A2}$$

where $\Delta\bar{r}_e$ is the period of the target regular set, $\bar{r}_e = e\Delta\bar{r}_e$, and Γ is a numeric arbitrary coefficient that defines the width of the reconstruction kernel. Similar to Rehfeld *et al*.,[42] $\Delta\bar{r}_e = L_x/(N_x - 1)$ was used, where N_x is the number of unique non-negative separations in the direction x and L_x is the maximum of $\bar{r}_n$. A discussion about the importance of the width parameter Γ and some guidelines for its selection can be found in the work of Rehfeld *et al*.[42]

The Fourier spatial transform of $\hat{W}_x(\bar{r}_e, \tau_m)^{(1)}$ is given by the convolution of the spectrum of $W_x(\bar{r}_n, \tau_m)$ with the characteristic spectrum of the kernel function. The sinc kernel causes the low-pass filtering of the original spectrum, where the cutoff spatial frequency decreases if Γ increases so that it is advisable to minimize Γ. On the other hand, the reconstruction procedure becomes unstable if the kernel width $\Gamma\Delta\bar{r}_e$ becomes much smaller than the maximum gap in the non-equidistant set $\bar{r}_n$. With the relatively sparse arrays of probes that were used in this study, the best compromise between the spectrum cutoff and the convergence of the analysis was found when $\Gamma = 2$. The same value was used in the benchmark test described by Rehfeld *et al*.[42]

Equation (A2) corresponds to the discrete sinc transform of $W_x(\bar{r}_n, \tau_m)$ from the irregular set of samples $\bar{r}_n$ to the regular set $\bar{r}_e$. It is easy to find that the coefficients of transform (A2) are not linearly independent if $\bar{r}_n$ are non-equidistant. This produces spurious contributions to the regularized correlation $\hat{W}_x(\bar{r}_e, \tau_m)^{(1)}$. The iterative procedure applied to a discrete signal comprises of the following steps:[36] (i) the discrete sinc transform is applied to the original irregularly sampled correlation in space, $W_x(\bar{r}_n, \tau_m)$, at each time separation τ_m, (ii) the inverse sinc transform is applied to the initial guess of the reconstructed correlation, $\hat{W}_x(\bar{r}_e, \tau_m)^{(1)}$. The result is $W_x(\bar{r}_n, \tau_m)^{(1)}$, which is defined on the original set of samples, $\bar{r}_n$. If the reconstructed signal is bandlimited to $\pi/\Delta\bar{r}_e$, the inverse transform does not produce additional errors because it is applied to the regularly spaced set $\bar{r}_e$, where the coefficients are linearly independent.[38] (iii) The residual at the first iteration $\varepsilon(\bar{r}_n, \tau_m)^{(1)}$ is found from the difference between $W_x(\bar{r}_n, \tau_m)^{(1)}$ and $W_x(\bar{r}_n, \tau_m)$, (iv) the residual is transformed to the regular set $\bar{r}_e$, to produce $\hat{\varepsilon}(\bar{r}_e, \tau_m)^{(1)}$, and (v) this is subtracted from the initial guess of $\hat{W}_x(\bar{r}_e, \tau_m)^{(1)}$ in order to reduce the effect of nonlinearities. The result is the improved estimate $\hat{W}_x(\bar{r}_e, \tau_m)^{(2)}$. The steps (ii)–(v) can be repeated until the residual becomes sufficiently small.

The inverse transform (step (ii)) of $\hat{W}_x(\bar{r}_e, \tau_m)^{(\kappa)}$ at the κth iteration is written as

$$W_x(\bar{r}_n, \tau_m)^{(\kappa)} = \sum_{e=-N_x+1}^{N_x-1} \hat{W}_x(\bar{r}_e, \tau_m)^{(\kappa)}\text{sinc}\left[\frac{2(\bar{r}_n - \bar{r}_e)}{\Gamma\Delta\bar{r}_e}\right]. \tag{A3}$$

The residual $\varepsilon(\bar{r}_n, \tau_m)^{(\kappa)}$ (step (iii)) is given by

$$\varepsilon(\bar{r}_n, \tau_m)^{(\kappa)} = W_x(\bar{r}_n, \tau_m)^{(\kappa)} - W_x(\bar{r}_n, \tau_m). \tag{A4}$$

The discrete transform applied to $\varepsilon(\bar{r}_n, \tau_m)^{(\kappa)}$ (step (iv)) produces the correction at the κth iteration,

$$\hat{\varepsilon}(\bar{r}_e, \tau_m)^{(\kappa)} = \sum_{n=-N_x+1}^{N_x-1} \varepsilon(\bar{r}_n, \tau_m)^{(\kappa)}\text{sinc}\left[\frac{2(\bar{r}_e - \bar{r}_n)}{\Gamma\Delta\bar{r}_e}\right]. \tag{A5}$$

The improved estimate at the iteration $\kappa + 1$ (step (v)) is

$$\hat{W}_x(\bar{r}_e, \tau_m)^{(\kappa+1)} = \hat{W}_x(\bar{r}_e, \tau_m)^{(\kappa)} - \varpi \hat{\varepsilon}(\bar{r}_e, \tau_m)^{(\kappa)}, \tag{A6}$$

where ϖ is an under-relaxation factor that controls the convergence, and $\hat{\varepsilon}(\bar{r}_e, \tau_m)^{(\kappa)}$ can serve as a convergence parameter.

The experimental results presented in this paper were obtained following the above procedure, where $\Gamma = 2$. The same procedure was repeated in the y-direction, where $\Delta\bar{r}_e = L_y/(N_y - 1)$. L_y and N_y have the same meaning of L_x and N_x, but in the y-direction. The convergence was considered to be reached when the maximum correction, $\hat{\varepsilon}(\bar{r}_e, \tau_m)^{(\kappa)}$, over the whole range of $(\bar{r}_e, \tau_m)$ became smaller than 1% of the maximum of the correlation function, $W_x(\bar{r}_n, \tau_m)$, the latter value being equal to 1. ϖ was set equal to 0.1 in order to reach the convergence in usually less than 200 iterations. Larger values of the under-relaxation factor made the iteration procedure unstable. The correction was found diverging in the region where the density of points $\bar{r}_n$ was smaller if a stricter convergence criterion was chosen, which was attributed to numerical instability. Fig. 3 shows the comparison between $W_x(\bar{r}_n, \tau_m)$ and the last iteration of $\hat{W}_x(\bar{r}_e, \tau_m)^{(\kappa)}$ for one single realization when $\tau_m = 0$, and $\kappa = 183$, with flow condition 11 (see Table II).

[1] J. W. Miles, "On the generation of surface waves by shear flows," J. Fluid Mech. **3**, 185 (1957).

[2] O. M. Phillips, "On the generation of waves by turbulent wind," J. Fluid Mech. **2**, 417 (1957).

[3] V. Klemas, "Remote sensing of coastal and ocean currents: An overview," J. Coastal Res. **28**, 576 (2012).

[4] A. Nichols, "Free surface dynamics in shallow turbulent flows," Ph.D. thesis, University of Bradford, Bradford (2015), Chap. 5, http://hdl.handle.net/10454/7345.

[5] I. Nezu and H. Nakagawa, *Turbulence in Open-Channel Flow. IAHR Monograph* (Balkema Publication, Rotterdam, 1993).

[6] M. Brocchini and D. H. Peregrine, "The dynamics of strong turbulence at free surfaces. Part 1. Description," J. Fluid Mech. **449**, 225 (2001).

[7] M. Rashidi, "Burst–interface interactions in free surface turbulent flows," Phys. Fluids **9**, 3485 (1997).

[8] S. Smolentsev and R. Miraghaie, "Study of a free surface in open-channel water flows in the regime from weak to strong turbulence," Int. J. Multiphase Flow **31**, 921 (2005).

[9] D. Yu and G. Tryggvason, "The free-surface signature of unsteady, two-dimensional vortex flows," J. Fluid Mech. **218**, 547 (1990).

[10] W.-T. Tsai, "A numerical study of the evolution and structure of a turbulent shear layer under a free surface," J. Fluid Mech. **354**, 239 (1998).

[11] R. Savelsberg and W. van de Water, "Experiments on free-surface turbulence," J. Fluid Mech. **619**, 95 (2009).

[12] I. Fujita, Y. Furutani, and T. Okanishi, "Advection features of water surface profile in turbulent open-channel flow with hemisphere roughness elements," Visualization Mech. Processes **1** (2011).

[13] J. Harband, "Three dimensional flow over a submerged object," J. Eng. Math. **10**, 1 (1976).

[14] J. Lighthill, *Waves in Fluids* (Cambridge University Press, Cambridge, 1978), p. 268.

[15] S.-J. Lee, G. T. Yates, and T. Y. Wu, "Experiments and analyses of upstream-advancing solitary waves generated by moving disturbances," J. Fluid Mech. **199**, 569 (1989).

[16] J. C. Burns, "Long waves in running water," in *Mathematical Proceedings of the Cambridge Philosophical Society* (Cambridge University Press, Cambridge, 1953), Vol. 49, p. 695.

[17] J. D. Fenton, "Some results for surface gravity waves on shear flows," IMA J. Appl. Math. **12**, 1 (1973).

[18] E. A. Caponi, H. C. Yuen, F. A. Milinazzo, and P. G. Saffman, "Water-wave instability induced by a drift layer," J. Fluid Mech. **222**, 207 (1991).

[19] V. I. Shrira, "Surface waves on shear currents: Solution of the boundary-value problem," J. Fluid Mech. **252**, 565 (1993).

[20] M. A. C. Teixeira and S. E. Belcher, "On the initiation of surface waves by turbulent shear flow," Dyn. Atmos. Oceans **41**, 1 (2006).

[21] V. Borue, S. A. Orszag, and I. Staroselsky, "Interaction of surface waves with turbulence: Direct numerical simulations of turbulent open-channel flow," J. Fluid Mech. **286**, 1 (1995).

[22] X. Guo and L. Shen, "Interaction of a deformable free surface with statistically steady homogeneous turbulence," J. Fluid Mech. **658**, 33 (2010).

[23] H. Nakagawa, I. Nezu, and H. Ueda, "Turbulence of open channel flow over smooth and rough beds," Proc. JSCE **1975**, 155.

[24] N.-S. Cheng, "Power-law index for velocity profiles in open channel flows," Adv. Water Resour. **30**, 1775 (2007).

[25] X. Zhang and C. S. Cox, "Measuring the two-dimensional structure of a wavy water surface optically: A surface gradient detector," Exp. Fluids **17**, 225 (1994).

[26] D. Dabiri and M. Gharib, "Simultaneous free-surface deformation and near-surface velocity measurements," Exp. Fluids **30**, 381 (2001).

[27] D. Dabiri, "On the interaction of a vertical shear layer with a free surface," J. Fluid Mech. **480**, 217 (2003).

[28] F. Moisy, M. Rabaud, and K. Salsac, "A synthetic schlieren method for the measurement of the topography of a liquid interface," Exp. Fluids **46**, 1021 (2009).

[29] M. Takeda, H. Ina, and S. Kobayashi, "Fourier-transform method of fringe-pattern analysis for computer-based topography and interferometry," J. Opt. Soc. Am. **72**, 156 (1982).

[30] P. J. Cobelli, A. Maurel, V. Pagneux, and P. Petitjeans, "Global measurement of water waves by fourier transform profilometry," Exp. Fluids **46**, 1037 (2009).

[31] A. Maurel, P. Cobelli, V. Pagneux, and P. Petitjeans, "Experimental and theoretical inspection of the phase-to-height relation in fourier transform profilometry," Appl. Optics **48**, 380 (2009).

[32] E. Herbert, N. Mordant, and E. Falcon, "Observation of the nonlinear dispersion relation and spatial statistics of wave turbulence on the surface of a fluid," Phys. Rev. Lett. **105**, 144502 (2010).

[33] P. Cobelli, A. Przadka, P. Petitjeans, G. Lagubeau, V. Pagneux, and A. Maurel, "Different regimes for water wave turbulence," Phys. Rev. Lett. **107**, 214503 (2011).

[34] Q. Aubourg and N. Mordant, "Nonlocal resonances in weak turbulence of gravity-capillary waves," Phys. Rev. Lett. **114**, 144501 (2015).

[35] M. A. Donelan, J. Hamilton, and W. H. Hui, "Directional spectra of wind-generated waves," Philos. Trans. R. Soc., A **315**, 509 (1985).

[36] K. Gröchenig, "A discrete theory of irregular sampling," Linear Algebra Appl. **193**, 129 (1993).

[37] P. Stoica and N. Sandgren, "Spectral analysis of irregularly-sampled data: Paralleling the regularly-sampled data approaches," Digital Signal Process. **16**, 712 (2006).

[38] S. Maymon and A. V. Oppenheim, "Sinc interpolation of nonuniform samples," IEEE Trans. Signal Process. **59**, 4745 (2011).

[39] S. Patil and V. P. Singh, "Effect of vertically logarithmic steady currents on shallow surface waves," Phys. Oceanogr. **18**, 133 (2008).

[40] K. V. Horoshenkov, A. Nichols, S. J. Tait, and G. A. Maximov, "The pattern of surface waves in a shallow free surface flow," J. Geophys. Res.: Earth Surf. **118**, 1864, doi: 10.1002/jgrf.20117 (2013).

[41] S. A. Kitaigordskii, V. P. Krasitskii, and M. M. Zaslavskii, "On Phillips' theory of equilibrium range in the spectra of wind-generated gravity waves," J. Phys. Oceanogr. **5**, 410 (1975).

[42] K. Rehfeld, N. Marwan, J. Heitzig, and J. Kurths, "Comparison of correlation analysis techniques for irregularly sampled time series," Nonlinear Processes Geophys. **18**, 389 (2011).